RSC Advances

PAPER

View Article Online
View Journal | View Issue

Cite this: *RSC Adv.*, 2022, **12**, 7210

Fabrication of a zinc oxide/alginate (ZnO/Alg) bionanocomposite for enhanced dye degradation and its optimization study†

Vasi Uddin Siddiqui, *[a] Afzal Ansari, [a] M. Taazeem Ansari,[a] Md. Khursheed Akram[b] and Weqar Ahmad Siddiqi *[a]

Received 13th December 2021
Accepted 23rd February 2022

DOI: 10.1039/d1ra08991a

rsc.li/rsc-advances

This paper studies a new response surface methodology (RSM) based on the central composite design (CCD) modeling method to optimize the photocatalytic degradation of methylene blue (MB) and methyl orange (MO) by using a synthesized ZnO/Alg bionanocomposite under UV irradiation. ZnO with different content of sodium alginate (Alg) (10, 20, and 30% by weight) has been synthesized by a one-step sol–gel method. Zinc oxide (ZnO) nanoparticles were impregnated on the alginate polymer. Various characterization techniques were used to describe the physical and chemical properties of each catalyst such as XRD, FTIR, UV-vis, PL, FESEM, Raman, and BET. The optimal catalyst for MB and MO photocatalytic degradation process was discussed mathematically as a function of catalyst dose, irradiation time, and MB and MO concentration, which was modeled by CCD-RSM based on a statistical model (quadratic regression) and an optimization process (ANOVA analysis). The photocatalytic degradation efficiency of 98% was achieved for the optimal conditions of a dye concentration of 20 mg L^{-1}, the catalyst dose of 0.34 g L^{-1}, and an irradiation time of 90 min at pH 6. The measurement result (R^2 = 0.9901) showed that the considered model is very suitable, and the selected CCD-RSM successfully optimized the photodegradation conditions of MB and MO.

1. Introduction

Dye effluent containing chemicals from the textile industry is one of the primary pollutants in the environment, causing harm to both humans and the environment.[1] Aside from being discharged into water resources, these dyes discolor the water and are hazardous to human health.[2] Other industries that produce dyed wastewater include cosmetics production, leather manufacture, medicines, paper manufacturing, and dye manufacturing plants.[3] Among the many organic compounds, methyl orange (MO) and methylene blue (MB) dyes are widely used in various industries including the textile,[4] plastic,[5] paper,[6] leather, cosmetic, pharmaceutical, and food industries.[7,8] These dyes are well-known for being highly toxic and having the potential to cause significant damage to the environment. Severe exposure to these dyes can cause the release of aromatic amines (such as benzoic acid and methylene) and can be carcinogenic.[9] In humans, it can cause increased heart rate, vomiting, cyanosis, and tissue necrosis.[10] Even at very low concentrations, their presence is highly visible and will have an impact on aquatic life as well as the food chain.[11] It will increase the level of BOD in the water and is harmful to aquatic life. Because these dyes do not degrade and are absorbed by plants, they may induce genetic abnormalities in future human generations.[12] Therefore, it is highly desirable to remove these pollutants from industrial wastewater before it can be safely disposed of for public health. The methods for removing color from industrial wastewater are not destructive; they are not considered inclusive approaches, and they just convert pollutants from the liquid to the solid phase.

Several research undertaken in recent years to eradicate these contaminants using optical catalysts has shown that photocatalytic degradation is environmentally benign, green, and free of secondary contamination. Pairs of electron holes are generated during exposure of light to photocatalyst that accelerates the reaction by participating in it. Also, photocatalysis is economic, non-toxic, consumes less energy, and can be reused. The most common nanostructure photocatalysts are nanoparticles, especially metal nanoparticles, and metal oxides such as TiO_2, ZnO, CuO, SnO_2, *etc.* which are intensively used due to its strong absorption in the UV and visible region.[13–17] So far, some of the materials used as photocatalysts to remove various pollutants are TiO_2 and ZnO and has been utilized in varied fields such as catalysis, solar energy conversion,

[a]*Department of Applied Sciences and Humanities, Faculty of Engineering and Technology, Jamia Millia Islamia, New Delhi, 110025, India. E-mail: vasi168968@st.jmi.ac.in; wsiddiqui@jmi.ac.in; Tel: +91-9045083437; +91-8800710689*

[b]*Applied Sciences and Humanities Section, University Polytechnic, Faculty of Engineering and Technology, Jamia Millia Islamia, New Delhi, 110025, India*

† Electronic supplementary information (ESI) available. See DOI: 10.1039/d1ra08991a

optoelectronics, and biolabeling.[18–20] Many areas can benefit from the eco-friendly qualities of nanoscale zinc oxide, which is affordable, non-toxic, and antibacterial.[21,22] It also possesses strong chemical and mechanical strength as well as a combination of suitable electrical and optical capabilities.[23] There are several applications for ZnO nanoparticles. For example, they are used as strong absorbers of ultraviolet rays and photocatalysts in burn creams and sunscreens, rubber, paints, electronic products, glass products, cosmetics, and health and pharmaceutical products.[24,25] Under UV irradiation, ZnO in an aqueous solution exhibits photo-instability and photocorrosion, which make it ineffective as a wastewater treatment photocatalyst. Many reports suggested that the photo-corrosion under UV light significantly diminishes photocatalytic activity.[6,26] Therefore, a surface modification of ZnO to enhance the usability for photocatalysis is needed by using a suitable polymer since polymer networks have been extensively researched as controlled for the preparation of nanomaterials. These methods provide an exact mechanism to change the size, shape, and three-dimensional arrangement of nanoparticles.[27,28] Alginic acid (alginate) is isolated from a brown marine alga (Phaeophycean) commonly found along the coasts and it has a unique process for gel formation and has been one of the most studied biological macromolecules for such techniques for many intriguing properties.[29] It is a linear polysaccharide that contains 1,4-linked β-D-mannuronic (M) and α-L-guluronic (G) acid residues placed in a nonregular block-wise order along the chain.[30] The physical characteristics and affinity of alginate for divalent metals are determined by the amount of M and G residues and their macromolecular structure.[31] The "egg-box" model describes how alginates can acquire an ordered shape in the presence of Ca^{2+} or other divalent cations by dimerization of the poly-G sequences.[32] Chain sequences of poly-M or mixed poly-MG terminate dimerization regions, and multiple separate chains may become interconnected, facilitating gel network development.[33]

Photocatalysis experiments depend on several parameters and for the large number of influencing factors, this seems to be difficult to perform and manage. Resulting, inappropriate and inconsistent results showed after performing these such experiments without a robust methodology. Therefore, statistical modeling and experimental design methodology are recommended to address and optimize such conditions. Maximizing yields with influencing parameters and understanding the interaction phenomenon are both goals in terms of optimizing yields. To enhance the yields (output) and reduced the number of experiments response surface methodology (RSM) is one of the most adopted methods during past years.[34] This method provides ample information by observing the effect of the interaction of influencing variables on the response on a run of a smaller number of experiments.[35] In this methodology, effects of the interaction of independent variables represented by the model equation. This is the reason it is also called multivariable analysis and a largely accepted technique in experimental design for the photocatalytic treatment of industrial effluents. Soni and his colleagues used Pluronic P123 as a template to prepare N-doped TiO_2 mesoporous (NTM) inorganic–organic hybrid thin films using an evaporative induced self-assembly route. Under visible light irradiation, the results demonstrated interesting photochemical bactericidal properties in comparison to the undoped TiO_2 film with no photocatalysis.[20] Mousa *et al.* reported another study in which the photodegradation of Methyl Orange (MO) organic dye was performed using three distinct aqueous plant extracts: pomegranate (Pom), *Beta vulgaris* (V.B), and Seder. They discovered that green-generated TiO_2 NPs had higher photocatalytic activity and efficiency in photodegrading MO in the presence of UV light than chemically synthesized TiO_2 NPs samples.[13] Another study reported on a simple method was used to prepare ZnO@SiO_2 nanomaterials for photocatalytic degradation of organic dyes methylene blue and eosin under UV light. In this study, the estimation of chemical oxygen demand (COD) for the dye solution before and after the photocatalytic reaction was found to be 97% in MB and 92% in eosin dye. Furthermore, the scavenger study results showed that the ZnO@SiO_2 nanomaterials outperformed bare silica in terms of photocatalytic properties due to their charge carrier and reactive hydroxyl radicals species.[36] The photocatalytic degradation of two organic dyes in aqueous solution under UV irradiation was investigated using a low-cost sol–gel wet chemical method to synthesize ZnS/SiO_2 photocatalyst. The photocatalytic degradation efficiencies of methylene blue and eosin were found to be approximately 97% after approximately 120 min of irradiation treatment over the ZnS/SiO_2 (15%) photocatalyst.[37] The degradation of MB and malachite green (MG) dyes using zinc oxide/polyaniline (ZnO/PANI) nanocomposite in aqueous medium under natural sunlight and UV light irradiation was investigated by Eskizeybek *et al.* and degrades both dye solutions (MB or MG) with 99% efficiency after 5 hours of irradiation under natural sunlight.[38] Chaker *et al.* modeled and optimized the degradation of MO dye by cerium-doped mesoporous ZnO by using RSM and optimized the three independent variables *viz.*, pH-solution, pollutant concentration, and catalyst dosage.[39] A similar methodology had been adopted by Hasan *et al.* to optimize the oxidative degradation of *p*-nitrophenol using as-synthesized ZnO/CuO/alginate bio-nanocomposite under visible sunlight irradiation. The degradation was achieved in 137 min, followed pseudo first-order kinetics for which ˙OH oxidative radicals were responsible for achieving the target with 98.32% efficiency.[40]

Therefore, this research focuses on two main objectives. The first is to synthesize ZnO nanostructures with different loading of alginate polymer and study its texture, structure, and optical properties. The second focus is to optimize the three parameters (pollutant concentration, catalyst dose, and irradiation time) that affect the photocatalytic activity of the synthesized catalyst for the photodegradation of MB and MO dyes under the UV irradiation using CCD-RSM. The effect of catalyst dosage parameters on the degradation performance of MB and MO will be carried out. It also allows determining the interaction between the parameters considered and the optimal conditions of the process.

2. Experimental details

2.1 Materials

In this experiment, ACS grade zinc sulfate heptahydrate ($ZnSO_4 \cdot 7H_2O$, ≥99%, CAS number: 7446-20-0 Merck), sodium salt of alginic acid from brown algae ($C_6H_7O_6Na$, with medium viscosity, CAS number: 9005-38-3, Merck), and sodium hydroxide pellets (NaOH, ≥95%, CAS number: 1310-73-2, Merck) were used as received. Methylene blue (MB, $C_{16}H_{18}ClN_3S$) and methyl orange (MO, $C_{14}H_{14}N_3NaO_3S$) dye was procured from Thermo Fisher Scientific (India) were used as model organic contaminants. Chemical structures of MO and MB are shown in Fig. S1.† All aqueous solutions were prepared using deionized water throughout the experiment.

2.2 Synthesis of ZnO/Alg bionanocomposite

In different wt% ratios, zinc sulfate (2 M), and sodium alginate were added with NaOH (4 M) during stirring. The reaction was continuously stirred at 80 °C for 4 h. Finally, the white precipitate obtained was filtered, washed with deionized water several times to remove impurities, and dried overnight in a hot air oven at 80 °C. Next, the dried sample was grounded into powder and calcined at 500 °C for 3 h for further characterization. ZA1, ZA2, and ZA3 were named for samples of varying wt% proportions of zinc and alginate at 10%, 20%, and 30%, respectively. Pure ZnO was also prepared under analogous conditions as mentioned above without adding alginate.

2.3 Instrumentations and characterizations

The structural properties and crystallinity of the synthesized nanomaterials were examined by using an advanced powder X-ray diffractometer (XRD, Rigaku) under the operating condition of 40 kV with monochromator Cu Kα radiation ($\lambda = 1.54$ Å) and 2θ (degree) ranging from 20° to 80°. Field emission scanning electron microscope (FE-SEM, Zeiss, Germany, model number sigma 500 VP) was used to study the surface morphology while the functional group analysis was done by Fourier transform infrared (FT-IR, PerkinElmer) spectra recorded using the sample pellets with KBr in a transmittance mode in 400–4000 cm^{-1} wavenumber range. The specific surface area and pore size distribution were analyzed by a Brunauer–Emmett–Teller (BET) surface area analyzer (Quanta Chrome Novae-2200) at 150 °C for 3 h. For optical properties, characterization was done by a double beam UV-vis spectrophotometer (Hitachi, model-U3900) and Raman spectrometer (LabRAM, Model no. HR800, JY). All photocatalytic experiments were also performed by a double beam UV-vis spectrophotometer (Hitachi, model-U3900). The photoluminescence (PL) study was done by a fluorescence spectrophotometer (Shimadzu, RF-5000) at an exciting wavelength of 350 nm to determine the energy structure of nanoparticles.

2.4 Photocatalytic experiment

Photocatalytic experiments of ZnO/Alg against MB (cationic) and MO (anionic) dyes were performed under UV light irradiation. In a known concentrations (MB concentration of 30 mg L^{-1} and MO concentration of 30 mg L^{-1}) of 50 mL dye solution, 20 mg photocatalytic dose was added at natural pH (pH = 6.0). To achieve adsorption–desorption equilibrium, the suspension was sonicated for 5 minutes and then slowly stirred in the dark for 40 min. After exposing the sample to a UV-C light source (40 W), 3 mL aliquots were extracted and centrifuged at predefined time intervals of up to 90 min. The absorbance of the supernatant was measured using a UV-vis spectrophotometer at $\lambda_{max} = 665$ nm (MB) and $\lambda_{max} = 464$ nm (MO) wavelengths to assess the extent and progress of dye degradation. All studies were carried out at room temperature (27 ± 2 °C). Eqn (1) was used to calculate the % photocatalytic degradation efficiency (D):

$$\% D = \left(1 - \frac{C_t}{C_o}\right) \times 100 \quad (1)$$

where C_o and C_t are the initial and after time t (min) concentration (mg L^{-1}) of dye, respectively.[41] A total of 1.0 mL of 30% H_2O_2 was added to all the experiments. The standard calibration curve for a known concentration of MB and MO dye is shown in Fig. S1,† and it was used for subsequent calculations under study.

2.5 Experimental design and optimization study

To optimize the photodegradation process and response surface modeling, the central composite experimental design (CCD) was adopted. The statistical software Design-Expert 13.0.1.0 (State-Ease, USA) was used to assess and interpret the experimental design. RSM optimized three independent parameters for the investigation: photocatalyst dosage (A, mg), dye concentration (B, mg L^{-1}), and reaction time (C, min). For all the trials, the CCD was used. Table 1 shows the levels and their values, whereas Table S1† (see the ESI†) shows the responses of the 17 combinations with six components, eight factors, and three replicates at a central point. The parameters and their values were determined based on previous experiment findings.[42–44] A second-order polynomial model was fitted to experimental data using multiple regression equations. The model employed second-order (quadratic) eqn (2), which is shown belo:[45,46]

$$Y = \beta_0 + \sum_{j=1}^{n} \beta_j X_j + \sum_{j=1}^{n} \beta_{jj} X_j^2 + \sum_{j=1}^{n-1} \sum_{i=1}^{n} \beta_{ji} X_j X_i \quad (2)$$

where Y is the predicted response variable (dye degradation, %), β_0 is the intercept, n is the number of factors studied, β_j, β_{jj} and

Table 1 Independent variables and their corresponding levels for experimental design

		Coded levels				
Independent variable	Factors	$-\alpha$	−1	0	1	$+\alpha$
Photocatalyst dosage (mg)	A	3.18	10	20	30	36.82
Dye concentration (mg L^{-1})	B	3.07	15	32	50	61.93
Reaction time (min)	C	12.73	40	80	120	147.27

β_{ji} are the linear (main effect), quadratic and interactive model coefficients, respectively, and X_j and X_i are the levels of the independent parameters considered.

2.6 Statistical analysis

Using Design-Expert Software (version 13.0.1.0), the experimental outcomes were statistically evaluated. The goodness of fit of the regression model was assessed using the coefficients of determination (R^2), the model F-value (Fischer variation ratio), and probability value (prob > F), as well as analysis of variance (ANOVA). To better understand the optimum dye degradation conditions on response variables, three-dimensional response plots were prepared using Design Expert Software (version 13.0.1.0).[47]

3. Results and discussion

3.1 Structural and morphological properties

As illustrated in Fig. 1, ZnO, ZA1, ZA2, and ZA3 have a crystal structure that can be seen by the XRD pattern. The Bragg reflections of the standard wurtzite structure ($P6_3mc$, JCPDS Card no. 36-1451) correspond well with all peaks indicating the formation of ZnO (Fig. 1). The miller index values (100), (002), (101), (102), (110), (103), (200), (112), (201), (004), and (202) equates well with 2θ values at 31.76°, 34.42°, 36.42°, 47.62°, 56.62°, 62.94°, 66.40°, 67.96°, 69.18°, 72.66° and 77.08° of the crystalline planes of ZnO (JCPDS 36-1451), respectively.[48] As a result of the following chemical processes, ZnO nanoparticles could be formed in the presence of alginate:[49]

$$Zn^{2+} + 4OH^- \rightarrow Zn(OH)_2^{4-} \quad (3)$$

$$Zn(OH)_2^{4-} \xrightarrow{\Delta} ZnO + 2H_2O + 2OH^- \quad (4)$$

The reaction first involved the formation of $Zn(OH)_2^{4-}$ precursor by reacting the Zn^{2+} ion with OH^- radical. Thus, forming the $[Zn_xO_y(OH)_z]^{(z+2y-2x)-}$ cluster where, x, y, and z represents the numbers of Zn^{2+}, O^{2-}, and OH^- within the crystal, respectively.[50] During the crystallization of ZnO, this cluster is integrated into the crystal lattice. In the presence of divalent metals, alginate poly G-sequences, on the other hand, tend to get ordered confirmation by dimerization, acting as a controlled environment for the formation of nano-sized particles.[33] The morphology changes in all cases, even though the XRD pattern (Fig. 1) corresponds to the standard structure of ZnO was consistent. The bionanocomposites ZA1, ZA2, and ZA3 have a small amorphous nature due to the intercalation of ZnO into the alginate matrix and functionalization with chains of alginate biopolymers. When compared to the standard values with lowered intensity values, the spectrum exhibits peaks with a shifted diffraction angle (values 2θ). Although the width of the size distribution was dependent on the amount (wt%) of

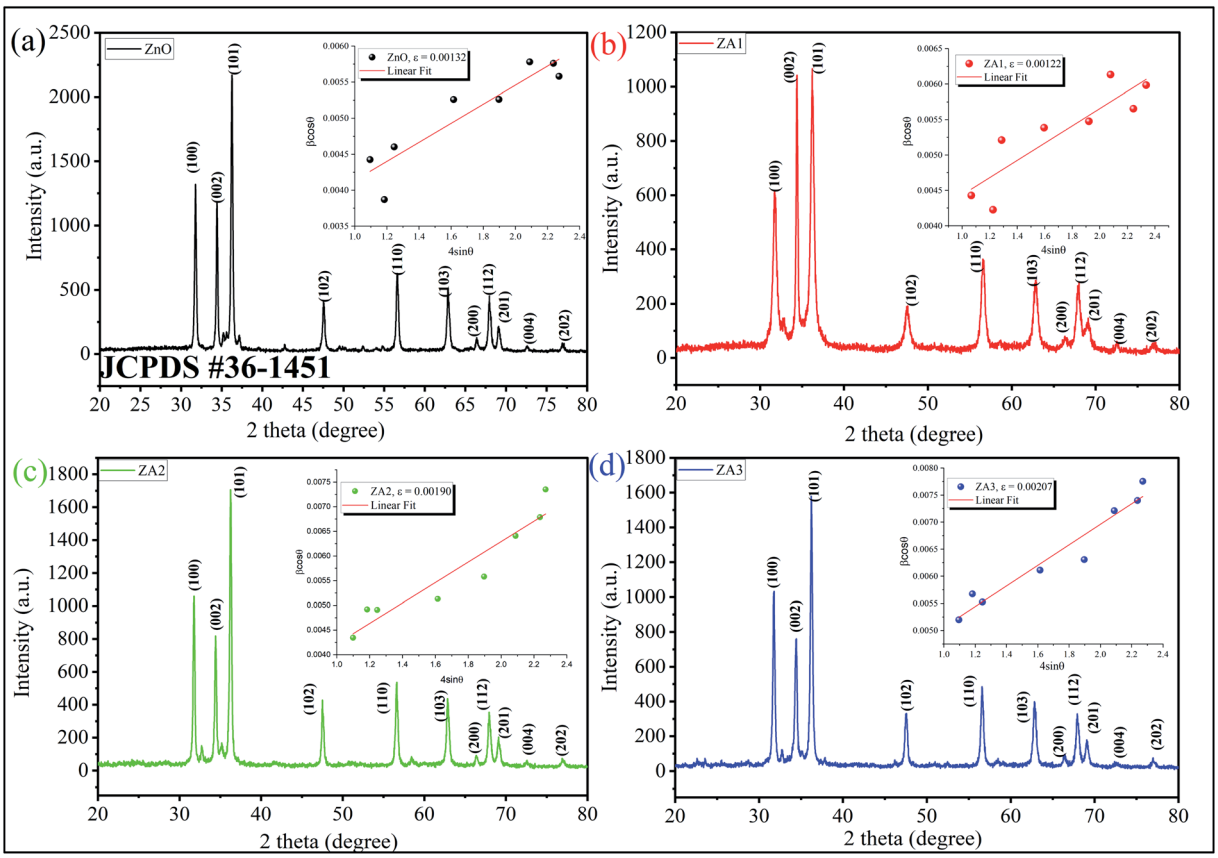

Fig. 1 XRD pattern and W–H plot (inset) of (a) ZnO, (b) ZA1, (c) ZA2 and (d) ZA3.

Table 2 Comparison of crystallite size, lattice strain, and dislocation density of ZnO, ZA1, ZA2, and ZA3 nanoparticles

	Average crystallite size D (nm)				
		Williamson–Hall analysis			
Samples	Scherrer's method (D)	D	Microstrain (ε)	Dislocation density (δ) lines per $m^2 \times 10^{15}$	Crystallinity (%)
ZnO	31.84	51.35	0.00132	0.99	59.33
ZA1	21.01	44.97	0.00122	2.22	60.36
ZA2	23.94	45.68	0.00190	1.74	57.36
ZA3	26.60	47.48	0.00207	1.41	59.36

alginate in the bionanocomposite, this showed that alginate can successfully limit the growth of ZnO nanoparticles. Scherrer's eqn (5) was also used to get the average crystallite size (D):

$$D = \frac{0.9\lambda}{\beta \cos \theta} \quad (5)$$

where λ is the Cu-Kα radiation of wavelength (1.5406 Å), β is the full width at half maximum (FWHM) in radians, and θ is the diffraction angle. Using eqn (5), the average crystallite size of ZnO, ZA1, ZA2, and ZA3 were found to be 31.84, 21.01, 26.60, and 23.94 nm, respectively. The broadening of the peak in ZnO/Alg arises due to strain caused by non-uniform lattice distortion and dislocation in the crystal phase due to the incorporation of Zn^{2+} into alginate polymer. The internal lattice strain eqn (6) and the Williamson–Hall (W–H) eqn (7) was used to calculate the crystallite size (D), and microstrain (ε) from the XRD pattern as modified Scherrer equation:[51]

$$\varepsilon = \frac{\beta_{hkl}}{4 \tan \theta} \quad (6)$$

$$\beta_{hkl} \cos \theta = \frac{0.9\lambda}{D} + 4\varepsilon \sin \theta \quad (7)$$

The least-square fit was used in $\beta_{hkl} \cos \theta$ *vs.* $4 \sin \theta$ for measuring the slope and intercept for calculating 'D' and 'ε' as shown in Fig. 1 (inset). The positive slope indicated the presence of strain in all as-synthesized nanomaterials and was higher in magnitude as size decreases suggesting the dislocation in lattice crystal. The dislocation caused by lattice strain was evaluated by using eqn (8):

$$\delta = \frac{1}{D^2} \quad (8)$$

where dislocation density (δ) is the length of the dislocation line per meter square of the crystal. As seen in Fig. 1, the XRD

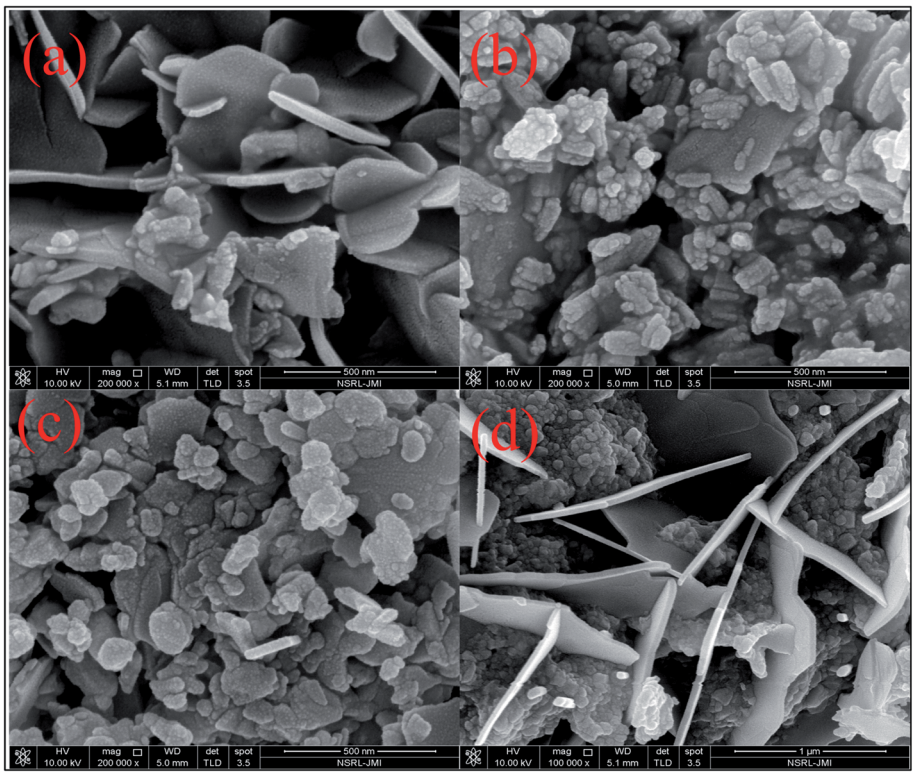

Fig. 2 FESEM images of (a) ZnO, (b) ZA1, (c) ZA2, and (d) ZA3.

pattern for ZA1 is showing that the (0 0 2) intensity is higher than the (1 0 0) plane but not so for pristine ZnO as well as for ZA2 and ZA3. This may be due to a higher number of lattice imperfections which is due to the increase of dislocation density and microstrain with the decrease of crystallite size in ZA1 after the small addition of alginate polymer.[52,53] This effect diminishes in ZA2 and ZA3 as the polymer loading increases in ZA2 and ZA3. Moreover, the ZnO (101) diffraction peak is much stronger than the ZnO (002) peak. This indicated that the formed ZnO nanocrystals have a preferential crystallographic (101) orientation.[54] Table 2 shows the comparative results from Scherrer's formula and W–H analysis analogous to previously reported literature.

The physicochemical features of the catalyst are known to be influenced by the surface shape, which provides vital information about the interaction of constituents.[55] The particle morphologies of all the synthesized ZnO and ZnO/Alg samples were subsequently studied using FESEM, and the results were displayed in Fig. 2.

3.2 Optical properties

Fig. 3(a) showed the UV-vis spectra of ZnO and ZnO/Alg bionanocomposite while the Tauc plot for the bandgap study showed in Fig. 3(b). The peak appeared at 387 nm corresponding to ZnO wurtzite hexagonal phase showed is analogous to the literature.[56] The alginate loading gives the peak to blue shift which could be understood by the nature of sodium alginate intercalated to ZnO.[57] This phenomenon of zinc oxide with alginate showed more efficient photocatalytic activity in the UV region. The presence of alginate in the synthesized sample increases the bandgap, indicating that Zn is incorporated into the alginate matrix. In XRD, this is shown as diffraction peak shifts. This can be explained by the so-called Brustein–Moss effect. Another factor leading to the widening of the bandgap is a change in the lattice parameter. Photocatalytic efficiency is dependent upon bandgap and increases with a decrease in the bandgap.

FTIR spectra as shown in Fig. 3(c) reveal the functional group associated with the ZnO, ZA1, ZA2, and ZA3 nanocomposite. Peaks at 424, 520, and 600 cm^{-1} (Zn–O bond stretching) and 1630 and 3416 cm^{-1} (–OH bending and stretching vibrations) are visible in the FTIR spectra of ZnO nanoparticles depicted in Fig. 3(c).[32] This –OH bond vibrations from alginate are due to the interaction with ZnO in ZA1, ZA2, and ZA3 shows small peak shifts around 3400 cm^{-1}.[30] The band at 1120 cm^{-1} is attributed to symmetric stretching of the C–O bond of CO_2, which is present in the air and absorbed on the surface.[31] Since carboxylic acid vibrational frequency has shifted slightly, it is likely

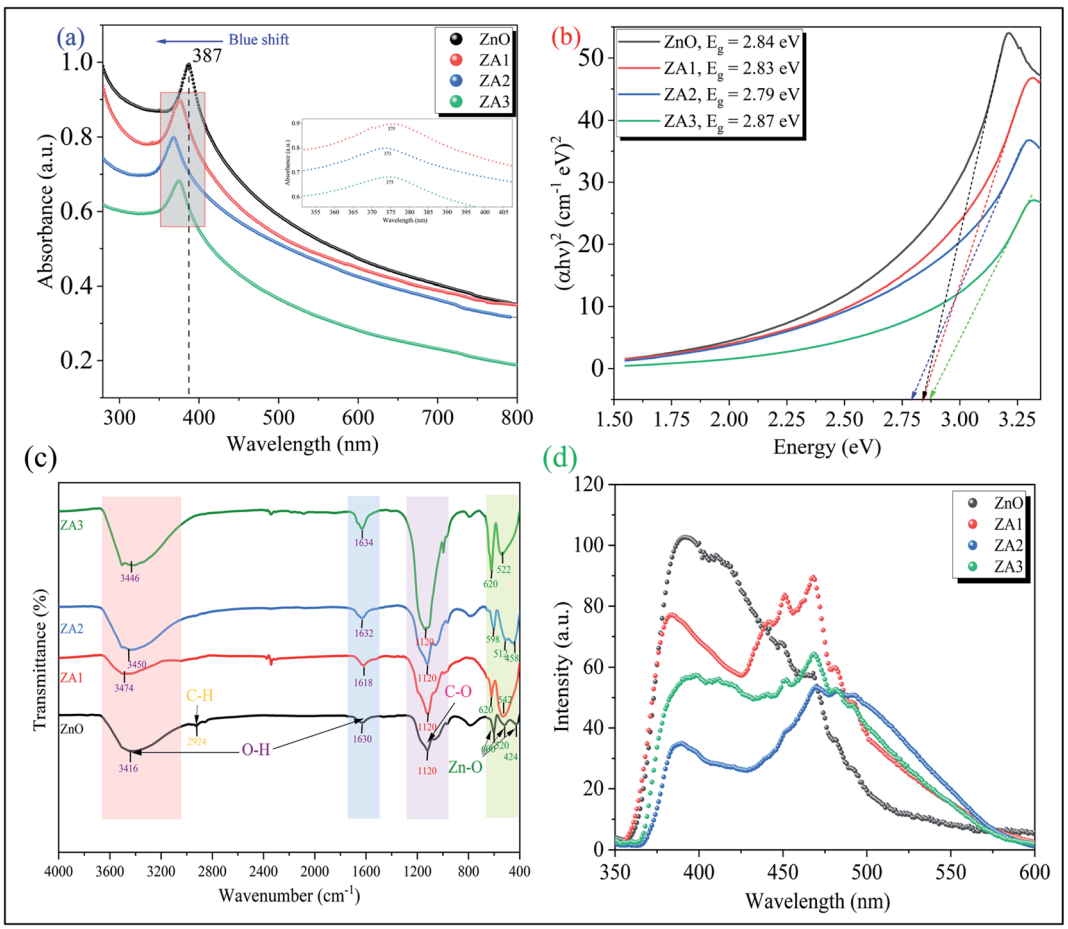

Fig. 3 (a) UV-vis spectra, (b) Tauc plot, (c) FT-IR spectra, and (d) PL spectra of ZnO, ZA1, ZA2, and ZA3.

that Zn^{2+} has been reduced and stabilized by oxygen electrons (lone pairs) forming a O–Zn-type lattices.[55] Intense peaks around 600–400 cm^{-1} found in ZA1, ZA2, and ZA3 bionanocomposite are attributed to ZnO nanoparticles.

Photoluminescence spectra were used to investigate the charge transfer and migration properties of pure ZnO and ZnO/Alg bionanocomposite. The intensity of PL emission is determined by the recombination of photo-excited electron–hole pairs; thus, lower, and higher PL emissions indicate more and less photogenerated charge carrier recombination. Fig. 3(d) shows the PL emission spectra of all synthesized photocatalysts. The resulting spectra can be divided into two parts: the band edge emission region, which has a wavelength range of 365 to 385 nm, and the second part, which has a wavelength range of 385 to 525 nm. The initial half of the emission spectrum is caused by conduction band electrons recombination with valence band holes. The second part emission region could be responsible for the defects that arises in the ZnO structure exist. In addition, pure ZnO shows a high-intensity peak, but when ZnO is mixed with alginate, the intensity of the PL spectrum is significantly reduced. Compared with pure ZnO, ZA1, and ZA3 samples, the emission intensity of the ZA2 bionanocomposite is greatly reduced. As a result, incorporating ZnO into alginate successfully reduced ZnO structure defects by minimizing surface defects. It is well known that defects are frequently concentrated on the surface of the material rather than being inhibited in the bulk phase due to the grafting of surfactant or dye molecules to the surface of the material. The combination of ZnO and alginate minimizes the emission intensity in our case. As a result, it can be deduced that the presence of ZnO on the surface of alginate minimizes ZnO surface defects and lowering charge carrier recombination.

3.3 BET analysis

From the N_2 adsorption–desorption isotherm study, it can be seen that the ZA2 has a large pore volume and a narrow pore size distribution. The samples showed a type IV hysteresis loop (IUPAC classification) for high P/P_0 values between 0.4 and 1.0, showing that ZA2 is porous (Fig. 4(b)). The surface area of the Brunauer–Emmett–Teller (BET) system was measured as 34.14 $m^2\ g^{-1}$. The Barrett–Joyner–Halenda (BJH) pore size distribution curve of ZA2 indicates a narrow pore size distribution ranging from ~2.5 to 27 nm, with an average pore diameter of ~14.9 nm (inset Fig. 4(a)) calculated using the Dubinin–Astakhov (DA) method.

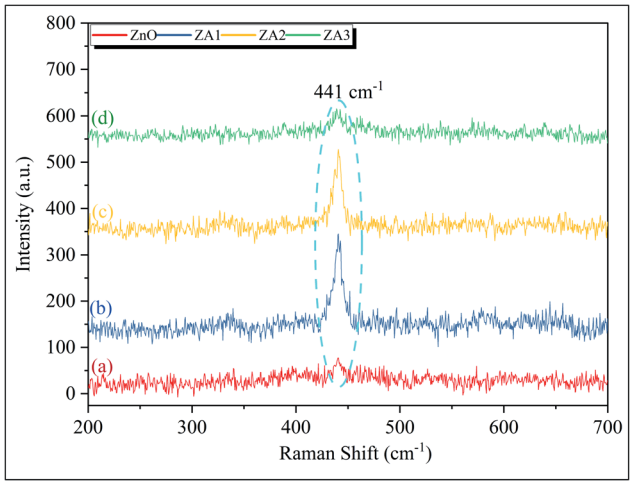

Fig. 5 Raman spectra for ZnO, ZA1, ZA2, and ZA3 sample.

3.4 Raman analysis

Raman scattering spectroscopy is used to investigate the structural disorder and defects of ZnO and ZnO/Alg bionanocomposite. The Raman-active optical–phonon E2 mode for wurtzite ZnO is attributed to a clear and significant peak at 440 cm^{-1} in Fig. 5.[58] Notably, no significant peak at 586 cm^{-1} was observed due to E11 mode, related oxygen vacancies, interstitial zinc, and their complexes.[48] As a result, the as-synthesized ZnO and ZnO/Alg bionanocomposite were of high-quality crystals with no oxygen vacancies on the surface.

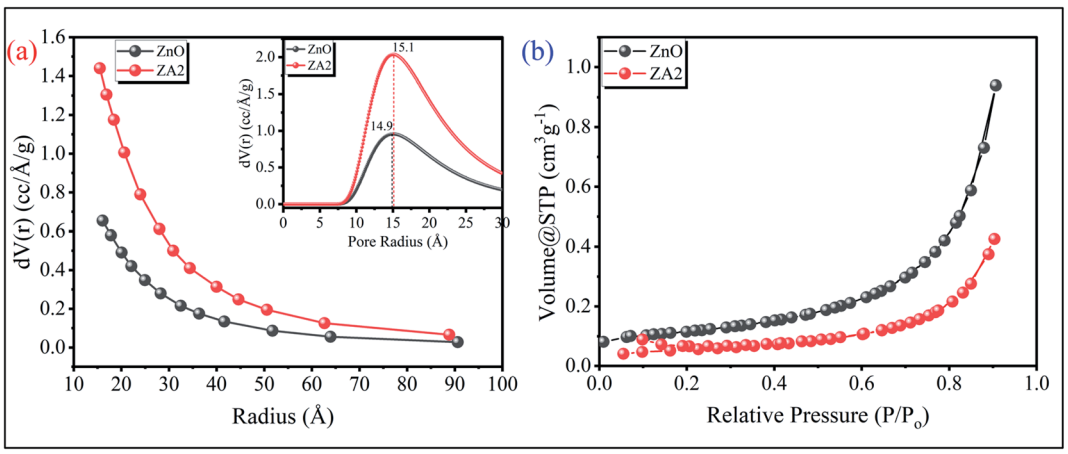

Fig. 4 (a) BJH pore size distribution (inset) DA pore radius, and (b) N_2 adsorption–desorption isotherm plots of the as-synthesized ZnO and ZnO/Alg bionanocomposite.

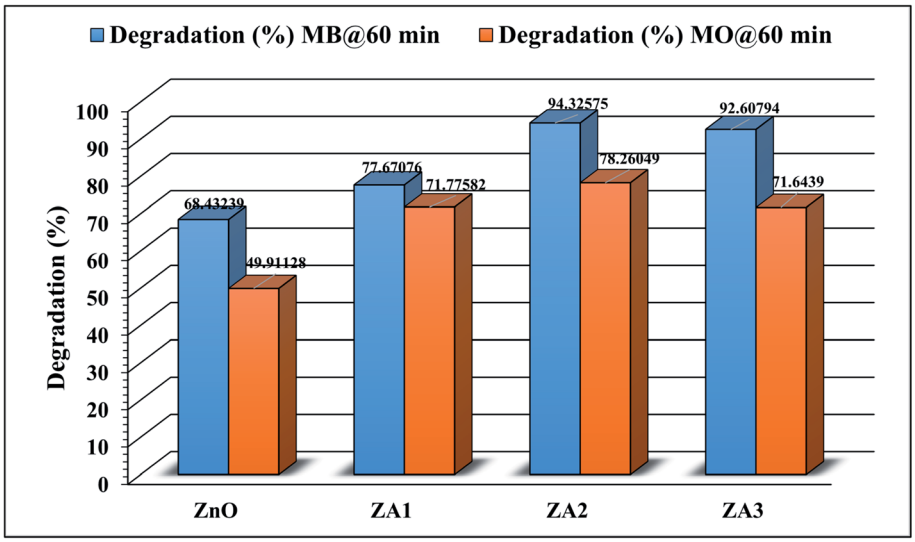

Fig. 6 Photocatalytic degradation of MB and MO over ZnO and ZnO/Alg bionanocomposite (dye concentration = 20 mg L^{-1}, catalyst dosage = 20 mg, irradiation time = 60 min).

3.5 Photocatalytic study

In this work, the photocatalytic activity of ZnO and ZnO/Alg bionanocomposites against the degradation of MB and MO dyes under UV light irradiation was studied. This work was carried out in two phases, the first part was carried out to select the photocatalyst among ZnO, ZA1, ZA2, and ZA3 for further experiments and the second part involved the study of optimization and statistical analysis for the selected sample.

3.5.1 Effect of ZnO and ZnO/Alg on degradation of dye. Preliminary studies reveal the degradation of MB and MO dyes as shown in Fig. 6 for ZnO and ZnO/Alg bionanocomposites. The results clearly indicate that ZA2 showed maximum degradation between ZnO and ZnO/Alg bionanocomposite with both dyes (MB and MO). This can be understood from the photoluminescence studies which showed the slowest rate of electron/hole recombination of ZA2 leading to better photocatalysis activity. The parameters included in this experiment were in good agreement with the previous literature. Since ZA2 showed maximum degradation, it was consequently used for all further experiments for optimization and modeling.

3.6 Modeling and statistical analysis

The response surface methodology with CCD was used to study the effect of independent parameters such as catalyst dosage, initial dye concentration, and reaction duration on photocatalytic degradation of MB and MO. Table 1 displays the input parameter levels in both coded and uncoded formats. A second-order polynomial equation was established based on the experimental design shown in Table S1† to represent the relationship between the independent factors and response. In terms of coded factors, the final eqn (9) and (10) for MB and MO, respectively, are as follows:

Table 3 ANOVA for photodegradation of MB dye[a]

Source	Sum of square	df	Mean square	*F*-value	*p*-value	Remark
Model	16 791.42	9	1865.713	241.8755	<0.0001	Significant
A – photocatalyst dosage	2948.016	1	2948.016	382.1879	<0.0001	
B – dye concentration	111.54	1	111.54	14.46032	0.006691	
C – reaction time	8997.225	1	8997.225	1166.422	<0.0001	
AB	187.6953	1	187.6953	24.33327	0.001689	
AC	4.485013	1	4.485013	0.581448	0.470655	
BC	31.00781	1	31.00781	4.019928	0.084993	
A^2	3223.687	1	3223.687	417.9265	<0.0001	
B^2	537.1736	1	537.1736	69.64048	<0.0001	
C^2	2603.661	1	2603.661	337.5449	<0.0001	
Residual	53.99467	7	7.713525			
Lack of fit	46.98781	5	9.397561	2.682386	0.293543	Not significant
Pure error	7.006867	2	3.503433			
Cor total	16 845.41	16				

[a] df – degree of freedom; R^2 = 0.9968; Pred R^2 = 0.9769; Adj R^2 = 0.9927.

Table 4 ANOVA for photodegradation of MO dye[a]

Source	Sum of square	df	Mean square	*F*-value	*p*-value	Remark
Model	17 571.67	9	1952.408	1344.425	<0.0001	Significant
A – photocatalyst dosage	1985.514	1	1985.514	1367.221	<0.0001	
B – dye concentration	17.49385	1	17.49385	12.04624	0.01039	
C – reaction time	9726.287	1	9726.287	6697.504	<0.0001	
AB	104.7628	1	104.7628	72.13949	<0.0001	
AC	0.400513	1	0.400513	0.275792	0.61569	
BC	7.125313	1	7.125313	4.906478	0.06233	
A^2	4531.269	1	4531.269	3120.224	<0.0001	
B^2	312.8834	1	312.8834	215.4509	<0.0001	
C^2	2654.362	1	2654.362	1827.789	<0.0001	
Residual	10.16558	7	1.452226			
Lack of fit	8.432512	5	1.686502	1.946264	0.373296	Not significant
Pure error	1.733067	2	0.866533			
Cor total	17 581.84	16				

[a] df degree of freedom; $R^2 = 0.9994$; Pred $R^2 = 0.9961$; Adj $R^2 = 0.9987$.

$$\%\text{Degradation (MB)} = 95.54 + 14.69 \times A - 2.85 \times B + 25.66 \times C + 4.84 \times AB + 0.7487 \times AC - 1.96875 \times BC - 16.91 \times A^2 - 6.90 \times B^2 - 15.19 \times C^2 \quad (9)$$

$$\%\text{Degradation (MO)} = 87.8355 + 12.057 \times A - 1.1317 \times B + 26.6869 \times C + 3.618 \times AB + 0.2237 \times AC - 0.94375 \times BC - 20.048 \times A^2 - 5.268 \times B^2 - 15.344 \times C^2 \quad (10)$$

And in terms of actual factors:

$$\%\text{Degradation (MB)} = -118.43 + 7.18 \times \text{photocatalyst dosage} + 0.9732 \times \text{dye concentration} + 2.2153 \times \text{reaction time} + 0.02767 \times \text{photocatalyst dosage} \times \text{dye concentration} + 0.001872 \times \text{photocatalyst dose} \times \text{reaction time} - 0.00281 \times \text{dye concentration} \times \text{reaction time} - 0.1691 \times \text{photocatalyst dosage}^2$$

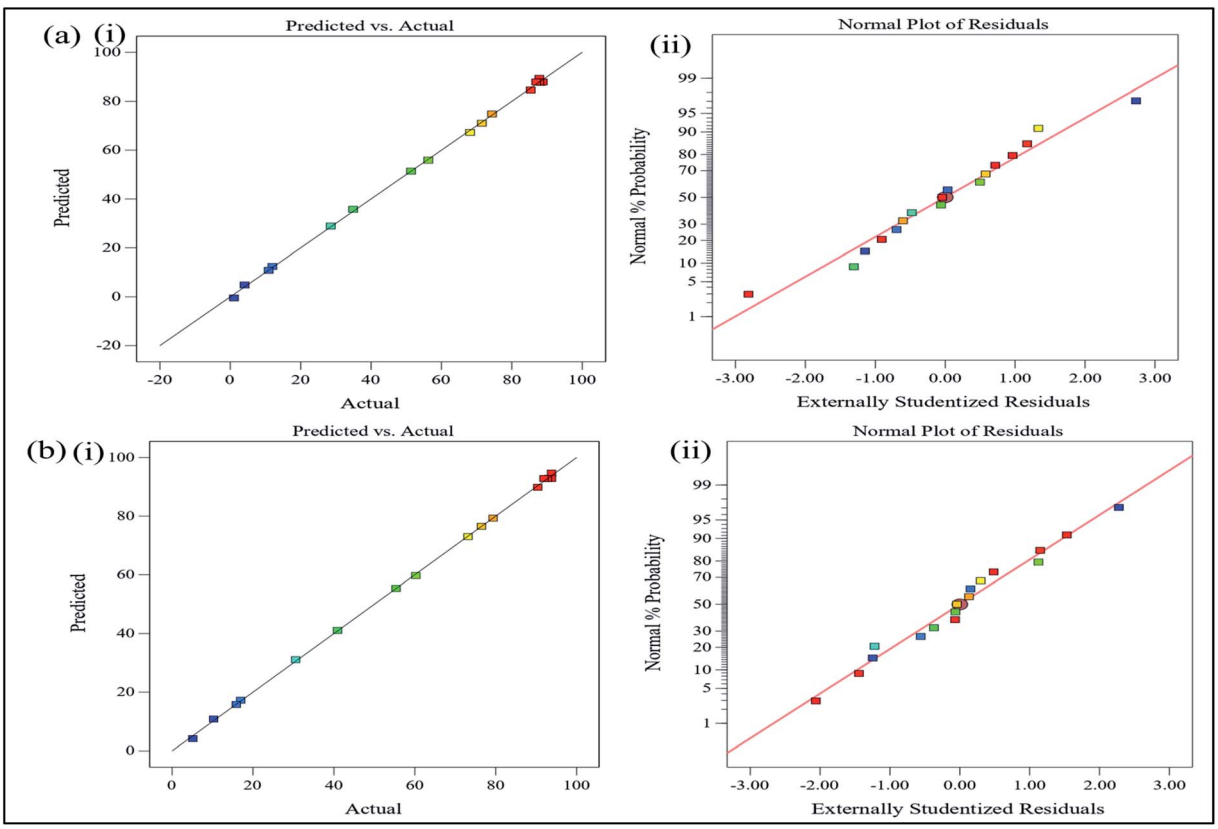

Fig. 7 (a) (i) Predicted *vs.* actual, (ii) normal probability plot values for photodegradation of MB and (b) (i) predicted *vs.* actual, (ii) normal probability plot values for photodegradation of MO.

$$- 0.02254 \times \text{dye concentration}^2 - 0.0095 \times \text{reaction time}^2 \quad (11)$$

$$\%\text{Degradation (MO)} = -136.463 + 8.50836 \times \text{photocatalyst dosage} + 0.7477 \times \text{dye concentration} + 2.2342 \times \text{reaction time} + 0.020679 \times \text{photocatalyst dosage} \times \text{dye concentration} + 0.000559 \times \text{photocatalyst dosage} \times \text{reaction time} - 0.00135 \times \text{dye concentration} \times \text{reaction time} - 0.20049 \times \text{photocatalyst dosage}^2 - 0.0172 \times \text{dye concentration}^2 - 0.00959 \times \text{reaction time}^2 \quad (12)$$

The adequacy of the model was evaluated using analysis of variance (ANOVA) for MB and MO, which are shown in Tables 3 and 4, respectively. Tables 3 and 4 describe the regression coefficients, R^2 values, and lack of fit. Each significance of coefficient was determined using the *F*-value and *p*-value. If Prob > *F* is less than 0.0500, the model terms are significant; if Prob > *F* is greater than 0.1000, the model terms are not significant.[47] The terms in Table 3 are significant according to Prob > *F* values for *A*, *B*, *C*, *AB*, A^2, B^2, C^2, but not for *AC* and *BC*. The terms in Table 4 are also significant for *A*, *B*, *C*, *AB*, A^2, B^2, and C^2, but not for *AC* and *BC*. For MB and MO degradation, the resulting F-value demonstrates that the irradiation time is the most important factor, followed by the catalyst dosage and dye concentration. Similarly, the *AB* interaction is the most prominent, followed by *BC* and *AC*. The resulting model has a "lack of fit *F* value" of 46.9878 for MB and 8.4325 for MO, suggesting that the "lack of fit" is "not significant", and the model is acceptable. Furthermore, coefficient of determination (R^2) values of 0.9968 for MB and 0.9994 for MO demonstrated that both simplified models could explain a significant percentage of the variance in the design space. The "Pred R^2" values of 0.9769 for MB and 0.9961 for MO are in good agreement with the respective "Adj R^2" values of 0.9927 and 0.9987. Furthermore, the signal-to-noise ratio computed by "Adeq Precision" is desirable for values greater than 4.[59] The "Adeq Precision" for MB and MO were 41.43 and 97.12, respectively. High values suggest a suitable signal and show the capacity of the model to explore the design space. Fig. 7(a)(i) and (b)(i) provide a comparison of predicted and actual response values for MB and MO, respectively. The high regression values for MB and MO of 0.9968 and 0.9994, respectively, indicate that the projected value was close to the actual value.

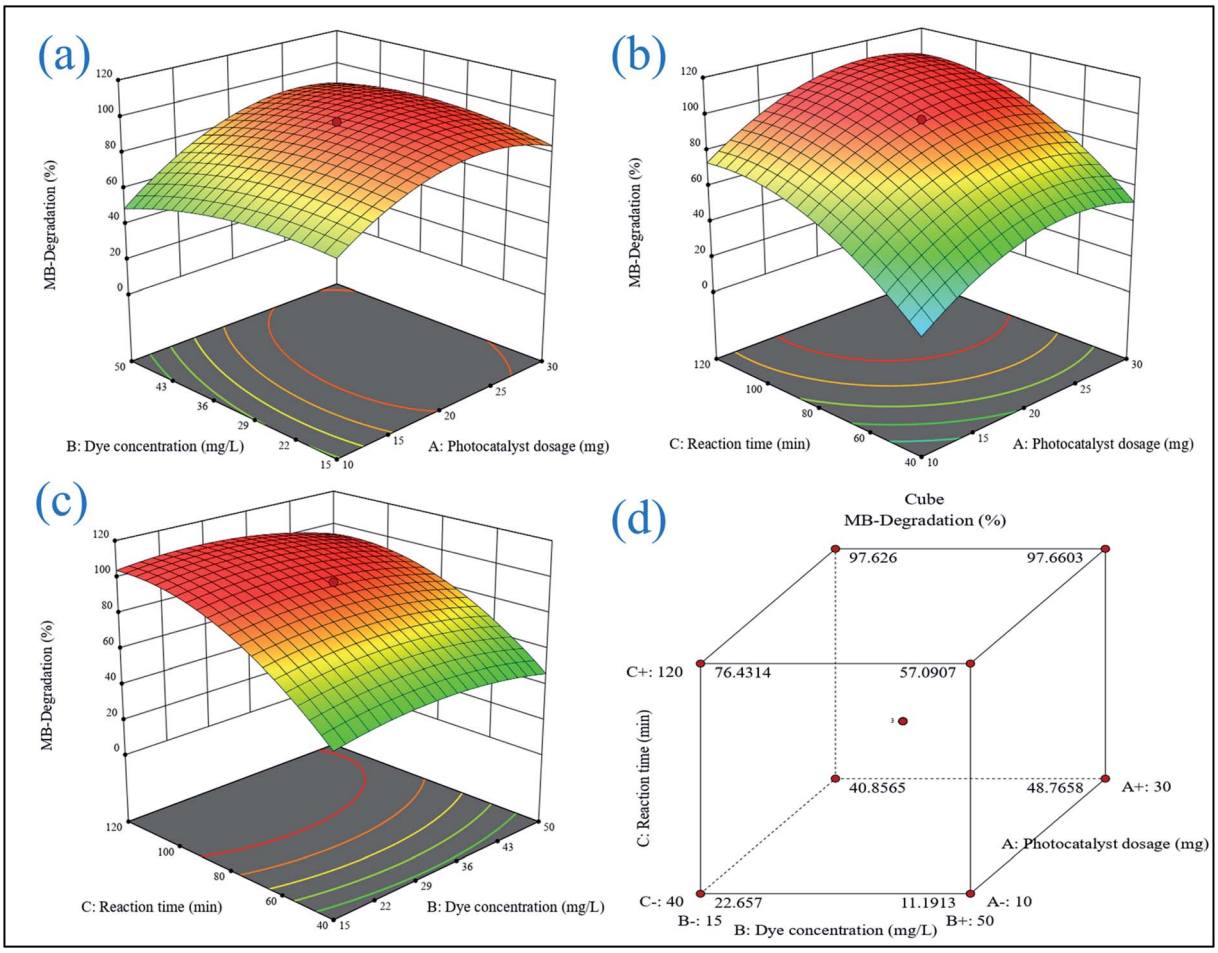

Fig. 8 3D response surface plots for MB showing the effects of (a) initial dye concentration and photocatalyst dosage, (b) reaction time and photocatalyst dosage, (c) initial dye concentration, reaction time, and coded response, (d) cumulative effect of all variable parameters.

The residuals, which are the differences between the experimental and projected values, were used to assess the model's appropriateness. This method identifies outliers and evaluates diagnostic charts such as normal probability and residuals plots. If the residuals have a normal distribution, the points on the normal probability plot should follow a straight line. Fig. 7(a)(ii) and (b)(ii) demonstrated that the residual was normally distributed since it resembled a straight line.

3.6.1 3D response surface plot analysis. A three-dimensional response surface plot was used to highlight the interaction between the two components in the photodegradation of MB and MO. Two parameters were changed within the experimental ranges in this technique, while one value remained constant.

3.6.1.1 Influence of dye concentration with catalytic dose. The percentage degradation of MB and MO dye is concentration-dependent, as shown in 3D response graphs of initial dye concentration and ZA2 NPs dose at 96 min contact time (Fig. 8(a) and 9(a)). With a fixed quantity of ZA2 catalyst and a higher dye concentration, more MB and MO molecules would quickly saturate the binding sites on the surface area. Because there are fewer adsorption sites, the rate of deterioration would be slowed.

3.6.1.2 Influence of catalytic dose with reaction time. Fig. 8(b) and 9(b) exhibit 3-D surface plots of MB and MO photodegradation as a function of sample loading and irradiation time, respectively. The circular shape of the 3D plot revealed that the interplay of sample loading concentration and irradiation time enhanced MB and MO photodegradation. The results showed that increasing the sample loading to approximately 20 mg improved the photodegradation of MB and MO during a short irradiation duration (40 min). As demonstrated, increasing the sample loading concentration and the irradiation time increased MB photodegradation. This could be understood by the fact that the longer the process was exposed to UV light, the more exposed the surface of the ZA2 photocatalyst was to hydroxyl radical, which photodegraded more MB and MO. As the sample loading increased, the photocatalytic activity slowed. Despite applying a longer duration of irradiation, a similar tendency was observed. This was because the extra ZA2 (>20 mg) served as a recombination center.[60]

3.6.1.3 Influence of dye concentration with reaction time. The effect of dye concentration on the photodegradation

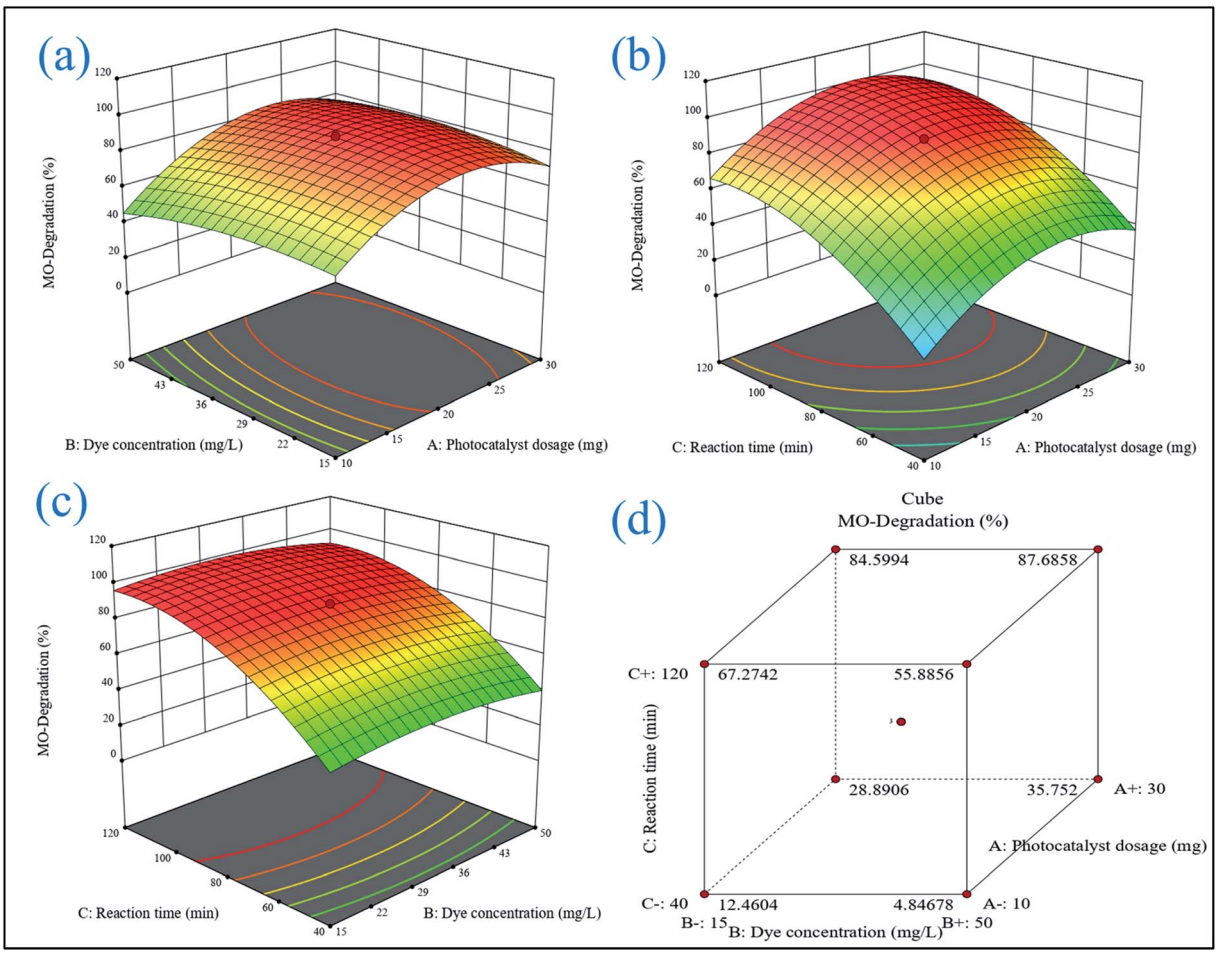

Fig. 9 3D response surface plots for MO showing the effects of (a) initial dye concentration and photocatalyst dosage, (b) reaction time and photocatalyst dosage, (c) initial dye concentration, reaction time, and coded response, (d) cumulative effect of all variable parameters.

Table 5 Optimization of the individual responses (d_i) to find the overall desirability response (D)

Name	Goal	Lower	Upper	Lower	Upper	Importance
A: photocatalyst dosage	Is in range	10	30	1	1	3
B: dye concentration	Is in range	15	50	1	1	3
C: reaction time	Is in range	40	120	1	1	3
MB-degradation	Maximize	6.12	97.81	1	1	5
MO-degradation	Maximize	1.04	88.79	1	1	5

performance at an initial pH of 6 is shown in Fig. 8(c) and 9(c). The outcome of the graph shows that the effectiveness of degradation was decreased by increasing the initial concentration of dye from 15 to 50 mg L^{-1} from 97 to 75% for MB and from 88 to 68% for MO. This could be explained as the presence of hydroxyl radical present on the surface might get interact with the dye molecules. Furthermore, the decrease in the degradation efficiency was due to the reducing the pathlength of photons entering the solution because of the intense color of dye concentration. As a result, fewer photons reached the

Table 6 Optimum values of the process parameters for constraint conditions and their experimental values

		MB degradation (%)		MO degradation (%)	
Factors	Optimum value	Predictive	Experimental	Predictive	Experimental
A: photocatalyst dosage	17.08	98.08	98.89	90.381	91.34
B: dye concentration	20.31				
C: reaction time	96.93				

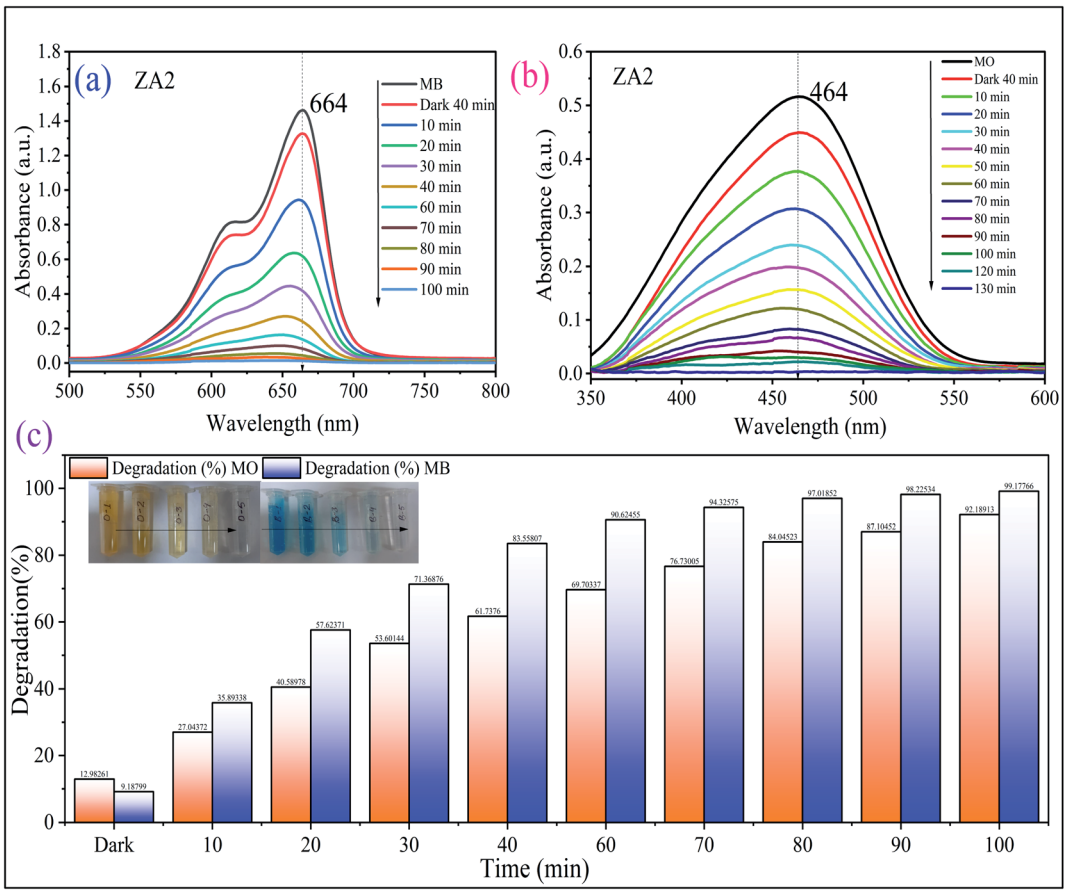

Fig. 10 Absorption spectra of photocatalytic degradation of (a) methylene blue and (b) methyl orange dyes over the optimized composition of ZA2 nanocomposite and its (c) bar graph.

surface of the nanocomposite.[61] Overall, the impact of these three parameters on MB and MO photodegradation was ranked irradiation time > catalyst dosage > dye concentration in declining order. The cubic contour plot in Fig. 8(d) and 9(d) depicted the cumulative influence of all variable factors on the percentage degradation of dye.

3.6.2 Process optimization. The ideal conditions for the degradation of MB and MO were determined using optimization based on the desire function. The location that optimizes the desirability function was found using numerical optimization tools. The application uses five goals to build desirability indices: none, maximum, minimum, target, and within range. Table 5 displays the criteria for all variables affecting the percentage of degradation. The weight, also known as significance, emphasizes upper and lower boundaries or target values. Because a higher degradation yield is the major goal of such studies, an "importance" value of 5 was selected as the maximum target. Based on the settings and bouncing, the best conditions for maximum MB and MO degradation efficiency (98.89% and 91.34%) were found to be a photocatalyst dosage of 17.08 mg, initial dye concentration of 20.31 mg L^{-1}, and reaction time of 96 min.

3.6.3 Model validation. A verification experiment was performed under optimal conditions to determine the applicability of the model for predicting the maximum percentage degradation of MB and MO dye. As indicated in Table 6, three repetition trials resulted in an average maximum degradation of 98.89% for MB and 91.34% for MO (Fig. 10). The good match between predicted and experimental results demonstrates the model's validity in simulating the photocatalytic degradation of MB and MO dye. Furthermore, MB and MO dye degradation by synthesized ZA2 catalyst displayed substantial photodegradation potential when compared to systems published in the literature (Table 7).

3.6.4 Kinetics and reusability study. A pseudo-first-order model was developed using the experimental data to examine the photocatalytic reaction kinetics of MB and MO degradation by the catalyst in greater detail (eqn (13)).[67]

$$\ln\frac{C_t}{C_o} = \ln\frac{A_t}{A_o} = -kt \quad (13)$$

where C_o (or A_o) represents the initial MB and MO concentration (or absorption), C_t (or A_t) represents the final MB and MO concentration (or absorption), and k represents the rate constant. The time-dependent changes and kinetics of MB and MO are presented in Fig. 11(a) respectively. The rate constant was calculated using the slope of the plot $\ln A_t/A_o$ *vs.* reaction time, as shown in Fig. 11(a). As a result, the MB and MO rate constants were determined to be 0.0522 and 0.0414 min^{-1}, respectively. The figure showed that the process of degradation follows Langmuir–Hinshelwood and pseudo-first-order kinetics.

To ensure the stability and reusability of the ZA2 bionanocomposite, the photocatalytic degradation of MB and MO was repeated five times with the same photocatalyst (Fig. 11(b)). In addition, Fig. 11(c) shows the UV-vis spectra of the ZA2 before and after the photocatalytic degradation reaction against MB and MO organic dye. The catalyst was centrifuged and cleaned with ethanol and water after each cycle before being used in photocatalytic degradation. The loss of ZA2 bionanocomposite during the separation and washing operations could explain the minor decrease in degradation percentage after each cycle. According to this finding, the ZA2 photocatalyst exhibits good photostability, reusability, and economic potential.

3.6.5 Photocatalytic mechanism. The photocatalysis of wastewater purification was based on the generation of electrons and holes in the presence of UV-visible light. These electron and hole photogenerations contribute to the formation of free radicals, which are extremely reactive species capable of breaking down the dye molecules and cleaning the water through chemical processes. The dye has a strong absorption peak of deionized water, but electrons and holes will break down the dye molecules after a photocatalytic process, resulting in a quick reduction in signal strength. Therefore, a reduction in the absorbent spectrum implies both photocatalytic activity and the purification of wastewater. To calculate the conduction

Table 7 Comparison of maximum dye degradation percentage of various nanoparticles

Catalyst	Dyes	Light source	Variables	Time (min)	Degradation (%)	References
ZnO–CuO (76% + 24%)	MB	UV with visible (sunlight)	Catalyst dosage = 1 mg, vol. = 8 mL, dye conc. = 7.5 mg L^{-1}	300	89%	42
Porous ZnO	MO	UV	Catalyst dosage = 0.2 g, dye conc. = 20 mg L^{-1}	120	96.30%	56
CuO/ZnO nanocomposites	MB	Visible	Catalyst dosage = 20 mg, dye conc. = 10 mg L^{-1}	120	98%	62
5% CuO loaded on ZnO	MB & MO	Visible	Catalyst dosage = 500 mg, vol. = 500 mL, dye conc. = 3×10^{-5} moles L^{-1}	120	97.2% & 87.7%	63
Cu_2O/ZnO	MO	Visible	Catalyst dosage = 0.1 g, vol. = 100 mL, dye conc. = 100 mg L^{-1}, pH = 3.8	240	98%	64
Cu-doped ZnO	MB & MO	UV	Catalyst dosage = 0.05 g, dye conc. = 0.03 mM, pH = 6.79 (MB) & 3.65 (MO)	180	57.5% & 60%	65
Al–Fe/ZnO	MB	Visible	Catalyst dosage = 0.05 g, dye conc. = 10 mg L^{-1}	75	90%	66
ZnO/Alg	MB & MO	UV light	Catalyst dosage = 17 mg, vol. = 50 mL, dye conc. = 20 mg L^{-1}, pH = 6	96	98.89% & 90.38%	This study

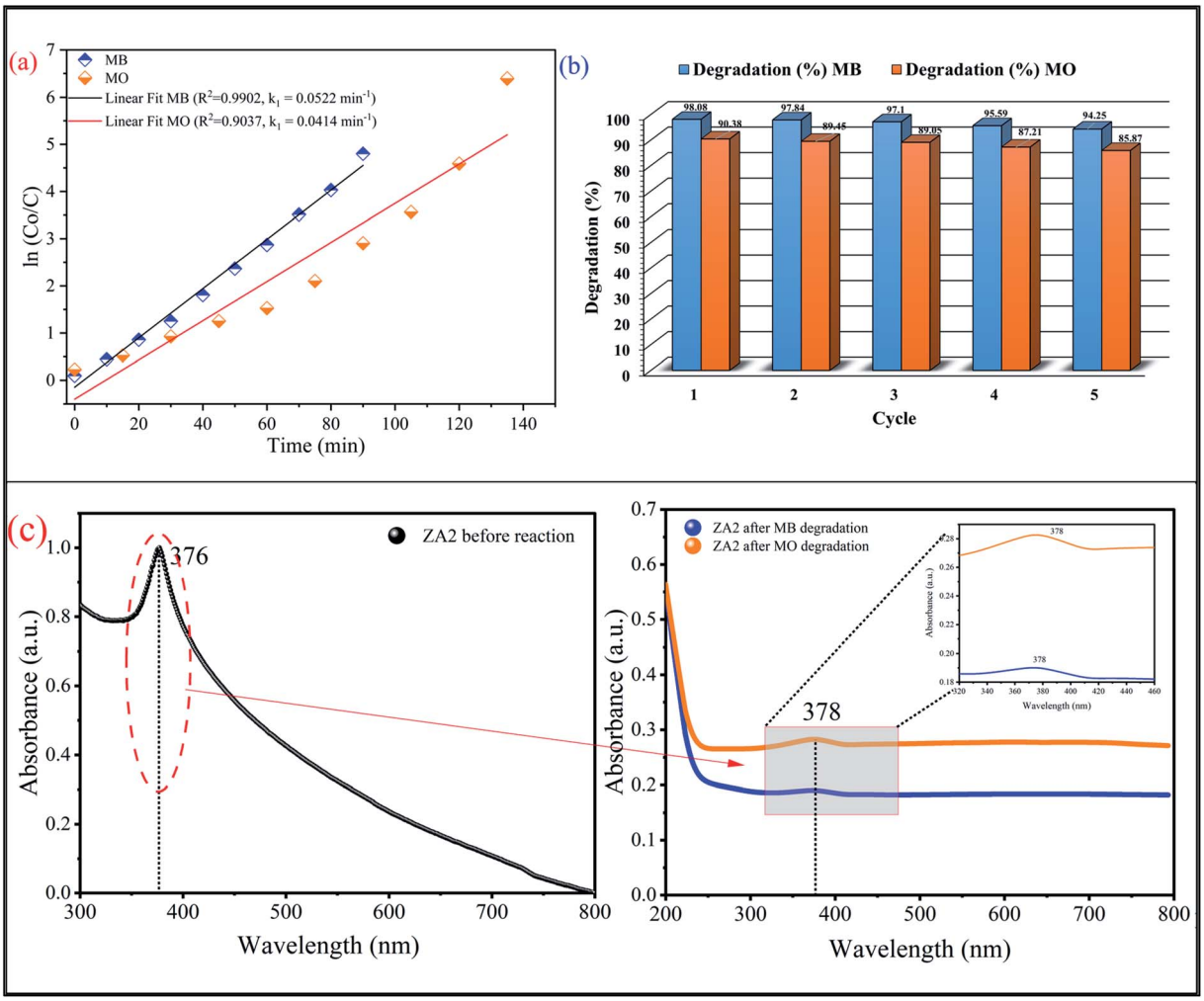

Fig. 11 (a) Pseudo-first order kinetics and (b) recyclability plot for photocatalytic degradation of MB and MO by ZA2 bionanocomposite, (c) UV-vis spectra of ZA2 before and after the reaction.

and valence band positions of the ZnO semiconductors at zero charges the following eqn (14) and (15) can be used.[68,69]

$$E_{vb} = X - E_e + 0.5E_g \quad (14)$$

$$E_{cb} = E_{vb} - E_g \quad (15)$$

where E_{vb} represents the valence band potential and X is the electronegativity of the semiconductor, which is the geometric mean of the electronegativity of the constituent atoms. Electronegativity values of ZnO is 5.79 eV.[70] On the hydrogen scale, E_e is the energy of free electrons (~4.5 eV), and E_g is the bandgap energy of semiconductors. The sample does not decolorize when exposed to visible light in the presence of pure ZnO because ZnO has a bandgap of 3.2 eV. The UV-vis region of electromagnetic radiation corresponds to the bandgap, and the absorbance spectrum of ZnO is flat in the visible range. Earlier studies have noted a similar pattern of behavior.[71] The following equation, based on previous findings, explains the possible photocatalytic mechanism.[42,72,73]

$$ZnO/Alg \xrightarrow{UV\ light} ZnO/Alg(e^- + h^+) \quad (16)$$

$$H^+ + OH^- \rightarrow H_2O \quad (17)$$

$$h^+ + OH^- \rightarrow OH^\bullet \quad (18)$$

$$e^- + O_2 \rightarrow {}^\bullet O_2^- \quad (19)$$

$$H_2O + {}^\bullet O_2^- \rightarrow OOH^\bullet + OH^- \quad (20)$$

$$2OOH^\bullet \rightarrow O_2 + H_2O_2 \quad (21)$$

$$OH^\bullet + {}^\bullet O_2^- + h_{vb}^+ + \text{pollutants} \rightarrow \text{degrade pollutants} \quad (22)$$

$$OH^\bullet + {}^\bullet O_2^- + h_{vb}^+ + \text{degrade pollutants} \rightarrow CO_2\uparrow + H_2O \quad (23)$$

When UV light is irradiated, electrons can move from the valence band of ZnO to the conduction band.[63] In comparison to ZnO, the ZnO/Alg materials also exhibit a blue shift in the absorption wavelength range, which might also help to increase photocatalytic performance in UV light presence. The O_2^* and OH^- radicals in MB interact with the S atoms of the C–S^+=C group, reducing the C=N bond. As a result of the

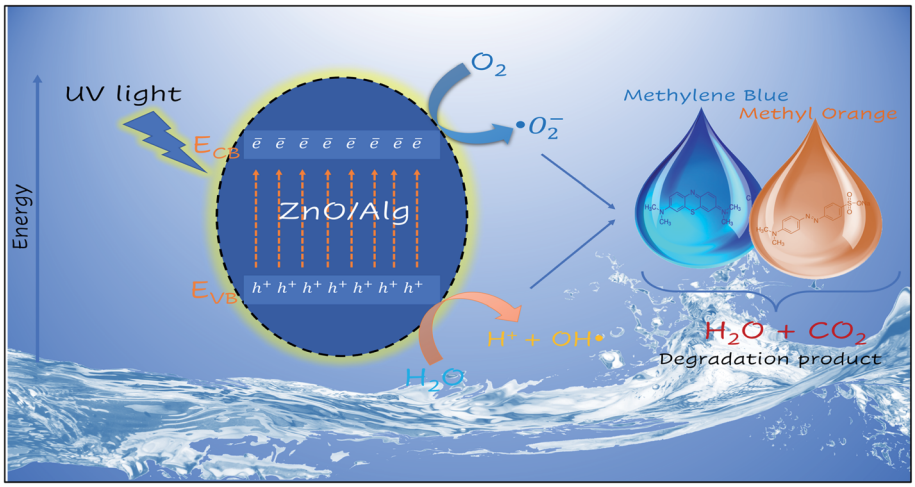

Fig. 12 Schematic representation of photocatalytic degradation of MB and MO over ZnO/Alg nanocomposite.

demethylation processes, CO_2, H_2O, and certain mineral species are produced as by-products. The photocatalytic degradation of MO, on the other hand, proceeds with the breaking of the N=N bond, causing the separation of the molecule.[74–78] The radicals then decompose the CH_3 group by attacking the CH_3–N–CH_3 group. Following that, one of the aromatic rings is released, followed by a series of intermediate processes that result in the final by-products of CO_2 and H_2O.[79–81] The surface charge of ZnO/Alg nanocomposite in an aqueous solution is another important factor that influences the adsorption of dye molecules on the catalyst surface and possibly the degradation mechanism. Furthermore, more characterization methods, such as GC-MS, LC-MS, ion chromatography (IC), and so on, could be used to gain more insights on the final products and intermediates of photocatalytic degradation, which could aid in the description of the degradation pathway. According to the UV-absorbance measurements, the ZnO/Alg bionanocomposite exhibits enhanced photocatalytic activity. A schematic representation of the photocatalytic mechanism is shown in Fig. 12. The photocatalytic activity decreases at a lower and greater concentration of alginate (ZA1 and ZA3) is mainly to the interaction between ZnO and alginate, which enhances the rate of charge recombination.[82] Simultaneously, a higher percentage of alginate samples (ZA3) have lower absorption values than the lower percentage of alginate (ZA1). As a result, the photocatalytic activity efficiency of ZA2 in direct or indirect degradation of organic dyes under UV light was enhanced.

4. Conclusions

ZnO/Alg is a high efficiency bionanocomposite material that may be used to decolorize water pollutants. It aids our progress toward a greener environment. The synthesis of ZnO/Alg bionanocomposite was carried out using a simple wet chemical method. Using X-ray diffraction analysis and the W–H plot, the crystalline size of all synthesized nanoparticles was found to be 44–51 nm from the Scherrer, 21–31 nm from the W–H plot, and the strain is 0.00122–0.00207. The FESEM investigation reveals the flakes-like structure of the as-synthesized ZnO/Alg nanocomposite. The obtained band gap is 2.79–2.87 eV, according to energy band structure investigations. The FTIR spectrum emphasizes the vibrational modes of ZnO and ZnO/Alg whereas Raman spectroscopy was used to analyze purity, crystallinity, and local vibration. The lower recombination rate indicated by the PL intensity indicates the slow recombination rate of photogenerated electron–hole pairs for ZA2 catalyst. The as-prepared ZnO/Alg composite outperforms pure ZnO in photocatalytic degradation of MB and MO dyes in UV light. The degradation is caused by the development of an intercalated network with alginate polymer that efficiently separates the photogenerated electron–hole pairs. After five cycles of repetition, the photocatalyst shows stable performance. A kinetic model of photocatalytic degradation over a heterogeneous catalyst with a first-order reaction is also suggested. The experimental data and this model are statistically compatible. The results of this study demonstrated that RSM based on CCD may be used to model and optimize photocatalytic dye degradation effectively. The analysis of variance revealed excellent correlation coefficients ($R^2 = 0.9968$ for MB, 0.9994 for MO, and Adj $R^2 = 0.9927$ for MB, 0.9987 for MO), indicating that the regression model was adequately adjusted to the experimental data. Irradiation duration was shown to have the most significant effect on MB and MO photodegradation, followed by photocatalyst loading, while dye concentration was found to have the least significant effect. The efficiency of the ZnO/Alg was determined to be 98.89% after 96 min of irradiation. The pseudo-first kinetic model also suggested the better photocatalytic degradation of MB than MO with a rate constant of 0.0522 min^{-1} and 0.0414 min^{-1}, respectively. The ZnO/Alg composite is a UV-light-driven active and stable catalyst that might be used to remediate dye contaminants in wastewater.

Author contributions

Vasi Uddin Siddiqui: conceptualization, methodology, visualization, formal analysis, investigation, software, data curation, writing – original draft, writing – review & editing. Afzal Ansari:

resources, writing – review & editing. M. Taazeem Ansari: resources, writing – review & editing. Md. Khursheed Akram: supervision, writing – review & editing. Weqar Ahmad Siddiqi: supervision, validation, writing – review & editing.

Conflicts of interest

The authors report no conflicts of interest.

Acknowledgements

Author Vasi Uddin Siddiqui is thankful to University Grants Commission (UGC) for the Non-NET fellowship. The authors are also thankful to the Central Instrumentation Facility (CIF) and Centre for Nanoscience and Nanotechnology, Jamia Millia Islamia, New Delhi for providing the characterization facility. Author Vasi Uddin Siddiqui also acknowledges the support of Prof. Masood Alam, Department of Applied Sciences and Humanities, Jamia Millia Islamia for providing the UV-Vis spectrophotometer facility.

References

1 A. Ahmad, S. H. Mohd-Setapar, C. S. Chuong, A. Khatoon, W. A. Wani, R. Kumar, *et al.*, Recent advances in new generation dye removal technologies: novel search for approaches to reprocess wastewater, *RSC Adv.*, 2015, **5**, 30801–30818, DOI: 10.1039/C4RA16959J.

2 H. Liu, C. Wang and G. Wang, Photocatalytic Advanced Oxidation Processes for Water Treatment: Recent Advances and Perspective, *Chem.–Asian J.*, 2020, **15**, 3239–3253, DOI: 10.1002/asia.202000895.

3 H. Lachheb, E. Puzenat, A. Houas, M. Ksibi, E. Elaloui, C. Guillard, *et al.*, Photocatalytic degradation of various types of dyes (Alizarin S, Crocein Orange G, Methyl Red, Congo Red, Methylene Blue) in water by UV-irradiated titania, *Appl. Catal., B*, 2002, **39**, 75–90, DOI: 10.1016/S0926-3373(02)00078-4.

4 M. Y. Nassar, E. I. Ali and E. S. Zakaria, Tunable auto-combustion preparation of TiO_2 nanostructures as efficient adsorbents for the removal of an anionic textile dye, *RSC Adv.*, 2017, **7**, 8034–8050, DOI: 10.1039/C6RA27924D.

5 A. Azam, O. Ahmed, H. Khan and A. Memic, Antimicrobial activity of metal oxide nanoparticles against Gram-positive and Gram-negative bacteria: a comparative study, *Int. J. Nanomed.*, 2012, **7**, 6003, DOI: 10.2147/IJN.S35347.

6 K. M. Lee, C. W. Lai, K. S. Ngai and J. C. Juan, Recent developments of zinc oxide based photocatalyst in water treatment technology: A review, *Water Res.*, 2016, **88**, 428–448, DOI: 10.1016/j.watres.2015.09.045.

7 K. Mageshwari, D. Nataraj, T. Pal, R. Sathyamoorthy and J. Park, Improved photocatalytic activity of ZnO coupled CuO nanocomposites synthesized by reflux condensation method, *J. Alloys Compd.*, 2015, **625**, 362–370, DOI: 10.1016/j.jallcom.2014.11.109.

8 L. Pérez-Ibarbia, T. Majdanski, S. Schubert, N. Windhab and U. S. Schubert, Safety and regulatory review of dyes commonly used as excipients in pharmaceutical and nutraceutical applications, *Eur. J. Pharm. Sci.*, 2016, **93**, 264–273, DOI: 10.1016/J.EJPS.2016.08.026.

9 K. Chung, Mutagenicity and carcinogenicity of aromatic amines metabolically produced from Azo Dyes, *J. Environ. Sci. Health, Part C: Environ. Carcinog. Ecotoxicol. Rev.*, 2000, **18**, 51–74, DOI: 10.1080/10590500009373515.

10 B. Lellis, C. Z. Fávaro-Polonio, J. A. Pamphile and J. C. Polonio, Effects of textile dyes on health and the environment and bioremediation potential of living organisms, *Biotechnol. Res. Innov.*, 2019, **3**, 275–290, DOI: 10.1016/J.BIORI.2019.09.001.

11 G. Crini, G. Torri, E. Lichtfouse, G. Z. Kyzas, L. D. Wilson and N. Morin-Crini, Dye removal by biosorption using cross-linked chitosan-based hydrogels, *Environ. Chem. Lett.*, 2019, **17**, 1645–1666, DOI: 10.1007/s10311-019-00903-y.

12 M. Soniya and G. Muthuraman, Recovery of methylene blue from aqueous solution by liquid–liquid extraction, *Desalin. Water Treat.*, 2015, **53**, 2501–2509, DOI: 10.1080/19443994.2013.866055.

13 S. A. Mousa, A. E. Shalan, H. H. Hassan, A. A. Ebnawaled and S. A. Khairy, Enhanced the photocatalytic degradation of titanium dioxide nanoparticles synthesized by different plant extracts for wastewater treatment, *J. Mol. Struct.*, 2022, **1250**, 131912, DOI: 10.1016/j.molstruc.2021.131912.

14 S. S. Soni, M. J. Henderson, J.-F. Bardeau and A. Gibaud, Visible-Light Photocatalysis in Titania-Based Mesoporous Thin Films, *Adv. Mater.*, 2008, **20**, 1493–1498, DOI: 10.1002/adma.200701066.

15 V. U. Siddiqui, A. Ansari, M. T. Ansari, M. K. Akram, W. A. Siddiqi, A. M. Alosaimi, *et al.*, Optimization of Facile Synthesized ZnO/CuO Nanophotocatalyst for Organic Dye Degradation by Visible Light Irradiation Using Response Surface Methodology, *Catalysts*, 2021, 11, DOI: 10.3390/catal11121509.

16 A. M. Al-Hamdi, U. Rinner and M. Sillanpää, Tin dioxide as a photocatalyst for water treatment: A review, *Process Saf. Environ. Prot.*, 2017, **107**, 190–205, DOI: 10.1016/J.PSEP.2017.01.022.

17 M. K. Ahmed, A. E. Shalan, M. Afifi, M. M. El-Desoky and S. Lanceros-Méndez, Silver-Doped Cadmium Selenide/Graphene Oxide-Filled Cellulose Acetate Nanocomposites for Photocatalytic Degradation of Malachite Green toward Wastewater Treatment, *ACS Omega*, 2021, **6**, 23129–23138, DOI: 10.1021/acsomega.1c02667.

18 A. M. Smith and S. Nie, Semiconductor Nanocrystals: Structure, Properties, and Band Gap Engineering, *Acc. Chem. Res.*, 2009, **43**, 190–200, DOI: 10.1021/ar9001069.

19 V. U. Siddiqui, A. Ansari, I. Khan, M. K. Akram and W. A. Siddiqi, Sol–gel synthesis of copper(II) oxide/alginate (CuO/Alg) bio-nanocomposite and effects of rapid thermal annealing on its properties and structure, *Mater. Res. Express*, 2019, **6**, 115095, DOI: 10.1088/2053-1591/ab4ace.

20 S. S. Soni, G. S. Dave, M. J. Henderson and A. Gibaud, Visible light induced cell damage of Gram positive bacteria by N-doped TiO_2 mesoporous thin films, *Thin Solid Films*, 2013, **531**, 559–565, DOI: 10.1016/j.tsf.2012.12.056.

21 N. Jones, B. Ray, K. T. Ranjit and A. C. Manna, Antibacterial activity of ZnO nanoparticle suspensions on a broad spectrum of microorganisms, *FEMS Microbiol. Lett.*, 2008, **279**, 71–76, DOI: 10.1111/j.1574-6968.2007.01012.x.

22 R. Brayner, S. A. Dahoumane, C. Yéprémian, C. Djediat, M. Meyer, A. Couté, *et al.*, ZnO Nanoparticles: Synthesis, Characterization, and Ecotoxicological Studies, *Langmuir*, 2010, **26**, 6522–6528, DOI: 10.1021/la100293s.

23 S. Kanimozhi, K. M. M. Prabu, S. Thambidurai and S. Suresh, Dye-sensitized solar cell performance and photocatalytic activity enhancement using binary zinc oxide–copper oxide nanocomposites prepared *via* co-precipitation route, *Ceram. Int.*, 2021, **47**, 30234–30246, DOI: 10.1016/j.ceramint.2021.07.203.

24 A. Kołodziejczak-Radzimska and T. Jesionowski, Zinc Oxide—From Synthesis to Application: A Review, *Materials*, 2014, **7**, 2833–2881, DOI: 10.3390/ma7042833.

25 L. V. Trandafilović, D. K. Božanić, S. Dimitrijević-Branković, A. S. Luyt and V. Djoković, Fabrication and antibacterial properties of ZnO–alginate nanocomposites, *Carbohydr. Polym.*, 2012, **88**, 263–269, DOI: 10.1016/j.carbpol.2011.12.005.

26 Y. Wang, R. Shi, J. Lin and Y. Zhu, Enhancement of photocurrent and photocatalytic activity of ZnO hybridized with graphite-like C_3N_4, *Energy Environ. Sci.*, 2011, **4**, 2922, DOI: 10.1039/c0ee00825g.

27 S. Pandey and S. B. Mishra, Sol–gel derived organic–inorganic hybrid materials: synthesis, characterizations and applications, *J. Sol-Gel Sci. Technol.*, 2011, **59**, 73–94, DOI: 10.1007/s10971-011-2465-0.

28 L. V. Trandafilović, R. K. Whiffen, S. Dimitrijević-Branković, M. Stoiljković, A. S. Luyt and V. Djoković, ZnO/Ag hybrid nanocubes in alginate biopolymer: Synthesis and properties, *Chem. Eng. J.*, 2014, **253**, 341–349, DOI: 10.1016/j.cej.2014.05.056.

29 K. Y. Lee and D. J. Mooney, Alginate: Properties and biomedical applications, *Prog. Polym. Sci.*, 2012, **37**, 106–126, DOI: 10.1016/j.progpolymsci.2011.06.003.

30 L. Motelica, D. Ficai, O. Oprea, A. Ficai, R.-D. Trusca, E. Andronescu, *et al.*, Biodegradable Alginate Films with ZnO Nanoparticles and Citronella Essential Oil—A Novel Antimicrobial Structure, *Pharmaceutics*, 2021, **13**, 1020, DOI: 10.3390/pharmaceutics13071020.

31 M. Thomas, G. A. Naikoo, M. U. D. Sheikh, M. Bano and F. Khan, Effective photocatalytic degradation of Congo red dye using alginate/carboxymethyl cellulose/TiO_2 nanocomposite hydrogel under direct sunlight irradiation, *J. Photochem. Photobiol., A*, 2016, **327**, 33–43, DOI: 10.1016/j.jphotochem.2016.05.005.

32 A. Salama, M. A. Diab, R. E. Abou-Zeid, H. A. Aljohani and K. R. Shoueir, Crosslinked alginate/silica/zinc oxide nanocomposite: A sustainable material with antibacterial properties, *Compos. Commun.*, 2018, **7**, 7–11, DOI: 10.1016/j.coco.2017.11.006.

33 R. Brayner, M.-J. Vaulay, F. Fiévet and T. Coradin, Alginate-Mediated Growth of Co, Ni, and CoNi Nanoparticles: Influence of the Biopolymer Structure, *Chem. Mater.*, 2007, **19**, 1190–1198, DOI: 10.1021/cm062580q.

34 R. H. Myers, D. C. Montgomery, and C. M. Anderson-Cook, *Response surface methodology: process and product optimization using designed experiments*, John Wiley & Sons, Inc., New Jersey, 4th edn, 2016.

35 N. Abbasi, S. A. Khan and T. A. Khan, Response surface methodology mediated process optimization of Celestine blue B uptake by novel custard apple seeds activated carbon/$FeMoO_4$ nanocomposite, *J. Water Process Eng.*, 2021, **43**, 102267, DOI: 10.1016/j.jwpe.2021.102267.

36 M. F. Abdel Messih, A. E. Shalan, M. F. Sanad and M. A. Ahmed, Facile approach to prepare ZnO@SiO_2 nanomaterials for photocatalytic degradation of some organic pollutant models, *J. Mater. Sci.: Mater. Electron.*, 2019, **30**, 14291–14299, DOI: 10.1007/s10854-019-01798-9.

37 M. F. Sanad, A. E. Shalan, M. A. Ahmed and M. F. A. Messih, The controlled synthesis and DFT investigation of novel (0D)–(3D) ZnS/SiO_2 heterostructures for photocatalytic applications, *RSC Adv.*, 2021, **11**, 22352–22364, DOI: 10.1039/D1RA02284A.

38 V. Eskizeybek, F. Sarı, H. Gülce, A. Gülce and A. Avcı, Preparation of the new polyaniline/ZnO nanocomposite and its photocatalytic activity for degradation of methylene blue and malachite green dyes under UV and natural sun lights irradiations, *Appl. Catal., B*, 2012, **119–120**, 197–206, DOI: 10.1016/j.apcatb.2012.02.034.

39 H. Chaker, A. E. Attar, M. Djennas and S. Fourmentin, A statistical modeling-optimization approach for efficiency photocatalytic degradation of textile azo dye using cerium-doped mesoporous ZnO: A central composite design in response surface methodology, *Chem. Eng. Res. Des.*, 2021, **171**, 198–212, DOI: 10.1016/j.cherd.2021.05.008.

40 I. Hasan, C. Shekhar, B. Sharfan II, R. A. Khan and A. Alsalme, Ecofriendly Green Synthesis of the ZnO-Doped CuO@Alg Bionanocomposite for Efficient Oxidative Degradation of *p*-Nitrophenol, *ACS Omega*, 2020, **5**, 32011–32022, DOI: 10.1021/acsomega.0c04917.

41 S. Merci, A. Saljooqi, T. Shamspur and A. Mostafavi, WO_3 nanoplates decorated with polyaniline and CdS nanoparticles as a new photocatalyst for degradation of imidacloprid pesticide from water, *Environ. Sci. Pollut. Res.*, 2021, **28**(27), 35764–35776, DOI: 10.1007/s11356-021-13031-4.

42 M. F. N. Taufique, A. Haque, P. Karnati and K. Ghosh, ZnO–CuO Nanocomposites with Improved Photocatalytic Activity for Environmental and Energy Applications, *J. Electron. Mater.*, 2018, **47**, 6731–6745, DOI: 10.1007/s11664-018-6582-1.

43 C. R. Rajith Kumar, V. S. Betageri, G. Nagaraju, G. H. Pujar, H. S. Onkarappa and M. S. Latha, One-pot green synthesis of ZnO–CuO nanocomposite and their enhanced photocatalytic and antibacterial activity, *Adv. Nat. Sci.: Nanosci. Nanotechnol.*, 2020, **11**, 015009, DOI: 10.1088/2043-6254/ab6c60.

44 M. Sharma, M. Poddar, Y. Gupta, S. Nigam, D. K. Avasthi, R. Adelung, *et al.*, Solar light assisted degradation of dyes

and adsorption of heavy metal ions from water by CuO–ZnO tetrapodal hybrid nanocomposite, *Mater. Today Chem.*, 2020, **17**, 100336, DOI: 10.1016/j.mtchem.2020.100336.

45 S. Dashamiri, M. Ghaedi, A. Asfaram, F. Zare and S. Wang, Multi-response optimization of ultrasound assisted competitive adsorption of dyes onto $Cu(OH)_2$-nanoparticle loaded activated carbon: Central composite design, *Ultrason. Sonochem.*, 2017, **34**, 343–353, DOI: 10.1016/j.ultsonch.2016.06.007.

46 R. M. Momina, S. Ismail and A. Ahmad, Optimization Study for the Desorption of Methylene Blue Dye from Clay Based Adsorbent Coating, *Water*, 2019, **11**, 1304, DOI: 10.3390/w11061304.

47 S. Mortazavian, A. Saber and D. E. James, Optimization of Photocatalytic Degradation of Acid Blue 113 and Acid Red 88 Textile Dyes in a UV-C/TiO_2 Suspension System: Application of Response Surface Methodology (RSM), *Catalysts*, 2019, **9**, 360, DOI: 10.3390/catal9040360.

48 R. Zhang, P.-G. Yin, N. Wang and L. Guo, Photoluminescence and Raman scattering of ZnO nanorods, *Solid State Sci.*, 2009, **11**, 865–869, DOI: 10.1016/j.solidstatesciences.2008.10.016.

49 Y. Zhang and J. Mu, Controllable synthesis of flower- and rod-like ZnO nanostructures by simply tuning the ratio of sodium hydroxide to zinc acetate, *Nanotechnology*, 2007, **18**, 075606, DOI: 10.1088/0957-4484/18/7/075606.

50 W.-J. Li, E.-W. Shi, W.-Z. Zhong and Z.-W. Yin, Growth mechanism and growth habit of oxide crystals, *J. Cryst. Growth*, 1999, **203**, 186–196, DOI: 10.1016/S0022-0248(99)00076-7.

51 A. Khorsand Zak, W. H. Abd Majid, M. E. Abrishami and R. Yousefi, X-ray analysis of ZnO nanoparticles by Williamson–Hall and size–strain plot methods, *Solid State Sci.*, 2011, **13**, 251–256, DOI: 10.1016/j.solidstatesciences.2010.11.024.

52 A. Begum, A. Hussain and A. Rahman, Effect of deposition temperature on the structural and optical properties of chemically prepared nanocrystalline lead selenide thin films, *Beilstein J. Nanotechnol.*, 2012, **3**, 438–443, DOI: 10.3762/bjnano.3.50.

53 A. Sanmugam, D. Vikraman, S. Venkatesan and H. J. Park, Optical and Structural Properties of Solvent Free Synthesized Starch/Chitosan–ZnO Nanocomposites, *J. Nanomater.*, 2017, **2017**, 1–8, DOI: 10.1155/2017/7536364.

54 P. Bindu and S. Thomas, Estimation of lattice strain in ZnO nanoparticles: X-ray peak profile analysis, *J. Theor. Appl. Phys.*, 2014, **8**, 123–134, DOI: 10.1007/s40094-014-0141-9.

55 S. Jurablu, M. Farahmandjou and T. P. Firoozabadi, Multiple-layered structure of obelisk-shaped crystalline nano-ZnO prepared by sol–gel route, *J. Theor. Appl. Phys.*, 2015, **9**, 261–266, DOI: 10.1007/s40094-015-0184-6.

56 N. Tripathy, R. Ahmad, H. Kuk, D. H. Lee, Y.-B. Hahn and G. Khang, Rapid methyl orange degradation using porous ZnO spheres photocatalyst, *J. Photochem. Photobiol., B*, 2016, **161**, 312–317, DOI: 10.1016/j.jphotobiol.2016.06.003.

57 H. J. Lee, J. H. Kim, S. S. Park, S. S. Hong and G. D. Lee, Degradation kinetics for photocatalytic reaction of methyl orange over Al-doped ZnO nanoparticles, *J. Ind. Eng. Chem.*, 2015, **25**, 199–206, DOI: 10.1016/j.jiec.2014.10.035.

58 R. Udayabhaskar and B. Karthikeyan, Optical and phonon properties of ZnO:CuO mixed nanocomposite, *J. Appl. Phys.*, 2014, **115**, 154303, DOI: 10.1063/1.4870447.

59 S. H. Dhawane, T. Kumar and G. Halder, Central composite design approach towards optimization of flamboyant pods derived steam activated carbon for its use as heterogeneous catalyst in transesterification of *Hevea brasiliensis* oil, *Energy Convers. Manage.*, 2015, **100**, 277–287, DOI: 10.1016/j.enconman.2015.04.083.

60 A. M. Tayeb, M. A. Tony and E. K. Ismaeel, Engineered nanostructured ZnO for water remediation: operational parameters effect, Box–Behnken design optimization and kinetic determinations, *Appl. Water Sci.*, 2019, **9**, 43, DOI: 10.1007/s13201-019-0921-0.

61 U. G. Akpan and B. H. Hameed, Parameters affecting the photocatalytic degradation of dyes using TiO_2-based photocatalysts: A review, *J. Hazard. Mater.*, 2009, **170**, 520–529, DOI: 10.1016/j.jhazmat.2009.05.039.

62 A. A. M. Sakib, S. M. Masum, J. Hoinkis, R. Islam and M. A. I. Molla, Synthesis of CuO/ZnO nanocomposites and their application in photodegradation of toxic textile dye, *J. Compos. Sci.*, 2019, **3**, 91, DOI: 10.3390/jcs3030091.

63 R. Saravanan, S. Karthikeyan, V. K. Gupta, G. Sekaran, V. Narayanan and A. Stephen, Enhanced photocatalytic activity of ZnO/CuO nanocomposite for the degradation of textile dye on visible light illumination, *Mater. Sci. Eng., C*, 2013, **33**, 91–98, DOI: 10.1016/j.msec.2012.08.011.

64 X. Wang, Y. Zhang, Q. Wang, B. Dong, Y. Wang and W. Feng, Photocatalytic activity of Cu_2O/ZnO nanocomposite for the decomposition of methyl orange under visible light irradiation, *Sci. Eng. Compos. Mater.*, 2019, **26**, 104–113, DOI: 10.1515/secm-2018-0170.

65 A. A. Shah, M. A. Bhatti, A. Tahira, A. D. Chandio, I. A. Channa, A. G. Sahito, *et al.*, Facile synthesis of copper doped ZnO nanorods for the efficient photo degradation of methylene blue and methyl orange, *Ceram. Int.*, 2020, **46**, 9997–10005, DOI: 10.1016/j.ceramint.2019.12.024.

66 N. R. Khalid, A. Hammad, M. B. Tahir, M. Rafique, T. Iqbal, G. Nabi, *et al.*, Enhanced photocatalytic activity of Al and Fe Co-doped ZnO nanorods for methylene blue degradation, *Ceram. Int.*, 2019, **45**, 21430–21435, DOI: 10.1016/j.ceramint.2019.07.132.

67 P. W. Koh, L. Yuliati and S. L. Lee, Kinetics and Optimization Studies of Photocatalytic Degradation of Methylene Blue over Cr-Doped TiO_2 using Response Surface Methodology, *Iran. J. Sci. Technol.*, 2019, **43**, 95–103, DOI: 10.1007/s40995-017-0407-6.

68 T. T. Minh, N. T. T. Tu, T. T. Van Thi, L. T. Hoa, H. T. Long, N. H. Phong, *et al.*, Synthesis of Porous Octahedral ZnO/CuO Composites from Zn/Cu-Based MOF-199 and Their Applications in Visible-Light-Driven Photocatalytic Degradation of Dyes, *J. Nanomater.*, 2019, **2019**, 1–16, DOI: 10.1155/2019/5198045.

69 M. Mahendiran, J. J. Mathen, K. M. Racik, J. Madhavan and M. V. A. Raj, Facile synthesis of n-ZnO@p-CuO

nanocomposite for water purification enhanced decolorization of methyl orange, *J. Mater. Sci.: Mater. Electron.*, 2019, **30**, 16099–16109, DOI: 10.1007/s10854-019-01980-z.

70 R. Darvishi Cheshmeh Soltani, A. R. Khataee and M. Mashayekhi, Photocatalytic degradation of a textile dye in aqueous phase over ZnO nanoparticles embedded in biosilica nanobiostructure, *Desalin. Water Treat.*, 2016, **57**, 13494–13504, DOI: 10.1080/19443994.2015.1058193.

71 E. D. Sherly, J. J. Vijaya and L. J. Kennedy, Visible-light-induced photocatalytic performances of ZnO–CuO nanocomposites for degradation of 2,4-dichlorophenol, *Chin. J. Catal.*, 2015, **36**, 1263–1272, DOI: 10.1016/S1872-2067(15)60886-5.

72 P. Sathishkumar, R. Sweena, J. J. Wu and S. Anandan, Synthesis of CuO–ZnO nanophotocatalyst for visible light assisted degradation of a textile dye in aqueous solution, *Chem. Eng. J.*, 2011, **171**, 136–140, DOI: 10.1016/j.cej.2011.03.074.

73 N. Siva, D. Sakthi, S. Ragupathy, V. Arun and N. Kannadasan, Synthesis, structural, optical and photocatalytic behavior of Sn doped ZnO nanoparticles, *Mater. Sci. Eng., B*, 2020, **253**, 114497, DOI: 10.1016/j.mseb.2020.114497.

74 P. A. Luque-Morales, A. López-Peraza, O. J. Nava-Olivas, G. Amaya-Parra, Y. A. Báez-López, V. M. Orozco-Carmona, *et al.*, ZnO Semiconductor Nanoparticles and Their Application in Photocatalytic Degradation of Various Organic Dyes, *Materials*, 2021, **14**, 7537, DOI: 10.3390/ma14247537.

75 M. A. Abu-Dalo, S. A. Al-Rosan and B. A. Albiss, Photocatalytic Degradation of Methylene Blue Using Polymeric Membranes Based on Cellulose Acetate Impregnated with ZnO Nanostructures, *Polymers*, 2021, **13**, 3451, DOI: 10.3390/polym13193451.

76 A. Houas, Photocatalytic degradation pathway of methylene blue in water, *Appl. Catal., B*, 2001, **31**, 145–157, DOI: 10.1016/S0926-3373(00)00276-9.

77 B. Albiss and M. Abu-Dalo, Photocatalytic Degradation of Methylene Blue Using Zinc Oxide Nanorods Grown on Activated Carbon Fibers, *Sustainability*, 2021, **13**, 4729, DOI: 10.3390/su13094729.

78 P. Benjwal, M. Kumar, P. Chamoli and K. K. Kar, Enhanced photocatalytic degradation of methylene blue and adsorption of arsenic(III) by reduced graphene oxide (rGO)-metal oxide (TiO_2/Fe_3O_4) based nanocomposites, *RSC Adv.*, 2015, **5**, 73249–73260, DOI: 10.1039/c5ra13689j.

79 P. A. Luque, H. E. Garrafa-Gálvez, O. Nava, A. Olivas, M. E. Martínez-Rosas, A. R. Vilchis-Nestor, *et al.*, Efficient sunlight and UV photocatalytic degradation of Methyl Orange, Methylene Blue and Rhodamine B, using *Citrus* × *paradisi* synthesized SnO_2 semiconductor nanoparticles, *Ceram. Int.*, 2021, **47**, 23861–23874, DOI: 10.1016/j.ceramint.2021.05.094.

80 V. V. Gawade, N. L. Gavade, H. M. Shinde, S. B. Babar, A. N. Kadam and K. M. Garadkar, Green synthesis of ZnO nanoparticles by using *Calotropis procera* leaves for the photodegradation of methyl orange, *J. Mater. Sci.: Mater. Electron.*, 2017, **28**, 14033–14039, DOI: 10.1007/s10854-017-7254-2.

81 X. Zheng, D. Zhang, Y. Gao, Y. Wu, Q. Liu and X. Zhu, Synthesis and characterization of cubic Ag/TiO_2 nanocomposites for the photocatalytic degradation of methyl orange in aqueous solutions, *Inorg. Chem. Commun.*, 2019, **110**, 107589, DOI: 10.1016/j.inoche.2019.107589.

82 X. Chen, Z. Wu, D. Liu and Z. Gao, Preparation of ZnO Photocatalyst for the Efficient and Rapid Photocatalytic Degradation of Azo Dyes, *Nanoscale Res. Lett.*, 2017, **12**, 143, DOI: 10.1186/s11671-017-1904-4.